ABSTRACT

NUMERICAL DETECTION OF COMPLEX SINGULARITIES IN TWO AND THREE DIMENSIONS

by
Kamyar Malakuti

Singularities often occur in solutions to partial differential equations; important examples include the formation of shock fronts in hyperbolic equations and self-focusing type blow up in nonlinear parabolic equations. Information about formation and structure of singularities can have significant role in interfacial fluid dynamics such as Kelvin-Helmholtz instability, Rayleigh-Taylor instability, and Hele-Shaw flow. In this thesis, we present a new method for the numerical analysis of complex singularities in solutions to partial differential equations. In the method, we analyze the decay of Fourier coefficients using a numerical form fit to ascertain the nature of singularities in two and three-dimensional functions. Our results generalize a well known method for the analysis of singularities in one-dimensional functions to higher dimensions. As an example, we apply this method to analyze the complex singularities for the 2D inviscid Burger's equation.

NUMERICAL DETECTION OF COMPLEX SINGULARITIES IN TWO AND THREE DIMENSIONS

by
Kamyar Malakuti

A Dissertation
Submitted to the Faculty of
New Jersey Institute of Technology and
Rutgers, The State University of New Jersey – Newark
in Partial Fulfillment of the Requirements for the Degree of
Doctor of Philosophy in Mathematical Sciences

Department of Mathematical Sciences, NJIT
Department of Mathematics and Computer Science, Rutgers-Newark

May 2009

APPROVAL PAGE

NUMERICAL DETECTION OF COMPLEX SINGULARITIES IN TWO AND THREE DIMENSIONS

Kamyar Malakuti

4/27/09

Michael Siegel, Dissertation Advisor — Date
Professor, Department of Mathematical Sciences, NJIT

4/27/09

Russel E. Caflisch, Committee Member — Date
Professor, Department of Mathematics, UCLA

4/27/2009

Lou Kondic, Committee Member — Date
Associate Professor, Department of Mathematical Sciences, NJIT

4/27/09

Jonathan H. Luke, Committee Member — Date
Professor, Department of Mathematical Sciences, NJIT

4/27/09

Demitrios T. Papageorgiou, Committee Member — Date
Professor, Department of Mathematical Sciences, NJIT

BIOGRAPHICAL SKETCH

Author: Kamyar Malakuti

Degree: Doctor of Philosophy

Date: May 2009

Date of Birth:

Place of Birth:

Undergraduate and Graduate Education:

- Doctor of Philosophy in Mathematical Sciences,
  New Jersey Institute of Technology, Newark, NJ, 2009
- Master of Science in Applied Mathematics,
  New Jersey Institute of Technology, Newark, NJ, 2007
- Master of Arts in Pure Mathematics,
  Kerman University, Kerman, Iran, 1994
- Bachelor of Science in Mathematics Education,
  Teachers Training University, Tehran, Iran, 1990

Major: Mathematical Sciences

Presentations and Publications:

K. Malakuti, R. E. Caflisch, N. P.Maung, M. Siegel, A. Virodov, "Numerical Detection of Complex Singularities in Two and Three Dimensions," in preparation.

K. Malakuti, "The Numerical Analysis of Singular Solutions to Partial Differential Equations," *SIAM Annual Meeting*, San Diego, July 7-11, 2008.

K. Malakuti, "The Numerical Analysis of Singular Solutions to Partial Differential Equations," *Applied Mathematics Seminar*, CUNY, Graduate Center, New York, May 2, 2008.

K. Malakuti, "The Numerical Analysis of Singular Solutions to Partial Differential Equations," *Summer Seminars Series*, NJIT, July 16, 2008.

K. Malakuti, "Tracing Complex Singularities," *Summer Seminars Series*, NJIT, July 12, 2007.

To the three women to whom I owe my life,
my grandmother, Parvin; my mother, Nasrin; and
my wife, Nadereh.

ACKNOWLEDGMENT

It has been such a long journey since I started my education in mathematics. In this mathematical journey I owe much to many of my professors, friends, and family members. The first one in this list is my thesis advisor, Prof. Michael Siegel. His knowledge, insight, and mathematical ability guide me through my doctoral research. His kindness and forgiveness have made him my dear friend as well as my advisor and mentor. My greatest gratitude goes to Prof. Michael Siegel.

I would like to thank Prof. Russel Caflisch, Prof. Wooyoung Choi, Prof. Lou Kondic, Prof. Jonathan H. Luke, and Prof. Demitrios Papageorgiou, for kindly serving on my defense committee. Prof. Caflisch also provided essential ideas for this thesis. Special thanks to Prof. Lou Kondic and Prof. Demitrios Papageorgiou, graduate advisors, for their caring and thoughtful advice throughout the doctoral program. Special Thanks to Prof. Daljit Ahluwalia, chairperson and Prof. Robert Miura former acting chair for all the efforts and cares they put into the Ph.D. program in mathematical sciences department at NJIT. I would like to thank Prof. Bruce Bukiet, Prof. Wooyoung Choi, Prof. Roy Goodman, and Prof. Joga Rao my dear friends for their academic supports throughout the doctoral program.

I am thankful to Prof Mehdi Radjabalipour, my M.A. thesis advisor for being such a great mathematician and mentor. special thanks to Prof. Mehdi Zahadi for his thoughtful advice throughout my Master program. I am also grateful to Prof. Masoud Farzan and Prof. Taher Ghasemi Honari who thought me how to be passionate about mathematics in my undergraduate program.

My dear friends, Mr. Navid Allahverdi, Mr. Liviu Mateescu, and Mr. Alexandr Virodov (all graduate students) helped me with different technical aspects of computing. I appreciate their helps greatly. I am also grateful to my good friends Prof. Bijan

Honari and Prof. Amir Togha for their helps to improve my mathematical intuition through endless discussions.

At the end, I would like to thank my family members, my parents Ali and Nasrin Malakuti, my dear friend and my brother in law Hossein Behnam, my wife and son Nadereh, and Sohrob, all of whom I love dearly, and I cannot thank them enough for their endless emotional support and love.

TABLE OF CONTENTS

LIST OF FIGURES

LIST OF FIGURES
(Continued)

Figure **Page**

CHAPTER 1

INTRODUCTION

Differential equations play important role in modeling many natural phenomenon. Analytical solutions to differential equations are known only in a small number of cases. Numerical solutions of differential equations have been an active and extensive research area in applied and pure mathematics. Some of the differential equations behave in such a way that their solutions show singular behavior. Here we consider an elementary example,

$$\frac{dy}{dt} = 1 + y^2, \qquad y(0) = 0,$$

where $y = \tan t$ is the solution. The solution exists only for $\frac{-\pi}{2} < t < \frac{\pi}{2}$. The solution reaches infinity at finite time hence we have a singular solution. This phenomenon is called blow-up in finite time.

Some of the well known examples of singularities that occur in solutions to partial differential equations (PDE) include the formation of shock fronts in hyperbolic equations [31], and self-focusing type blow up in nonlinear parabolic equations [41], [43]. Detecting a singular solution of a PDE is important from a theoretical point of view since it has to do with the well-posedness of the problem, which is one of the most important questions about any PDE. In a numerical calculation, detecting the presence of singular solutions of a differential equation is important as well since at space-time point of singularity, refining the mesh size may not result in convergence of the numerical solution.

1.1 Examples of Singularity Formation in Interfacial Fluid Dynamics

There are a number of important examples of singularity formation in interfacial fluid dynamics. The classical examples are Kelvin-Helmholtz instability, Rayleigh-Taylor instability and Hele-Shaw flow. For the case of Kelvin-Helmholtz instability [15],

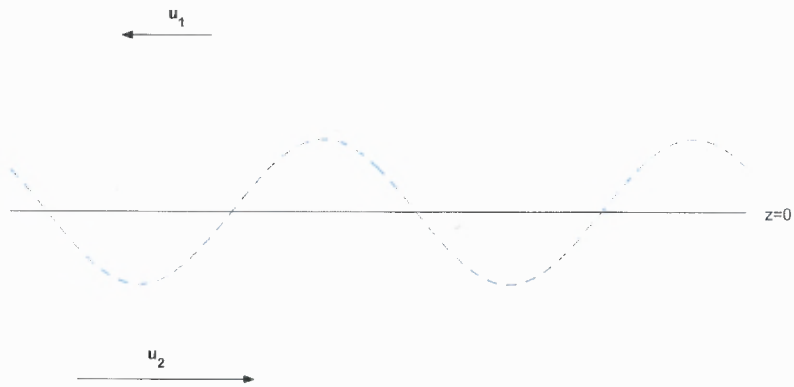

Figure 1.1 Two inviscid irrotational fluids with across the interface velocity difference.

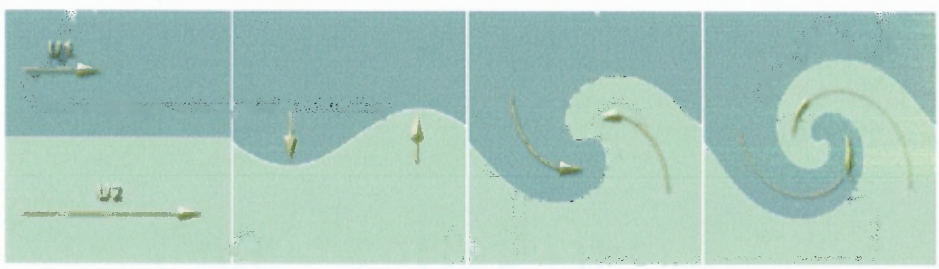

Figure 1.2 The phenomenon of rolling up of the interface in Kelvin-Helmholtz instability (Brockmann) [34].

there is a velocity jump across the interface between two inviscid irrotational fluids (for example water and air) which is illustrated in Figure 1.1. Assume the velocity of the upper fluid is $\mathbf{u}_1$ and the velocity of the lower one is $\mathbf{u}_2$. The interface separating the two fluids, at which point there is a jump in velocity, is a vortex sheet. A sinusoidal perturbation of a flat interface is unstable. Pressure in concavities is higher than pressure in convexities (see arrows in Figure 1.2 for an illustration of the direction of

pressure at the interface). This implies that the amplitude of the perturbation on the interface grows and the upper part of the sheet is carried and stretched by upper fluid while similarly, the lower part of the sheet is carried and stretched by lower fluid, as shown on the right hand side of Figure 1.2. As a consequence, the interface rolls up in a direction consistent with the direction of circulation at the interface, which in this case is out of the plane.

The initial-value problem for perturbations of a flat, constant strength vortex sheet is ill-posed [28], [22], [25], [13], and [39] and the vortex sheet develops finite time singularity. To have a sense of this, assume

$$z(\Gamma, t) = x(\Gamma, t) + iy(\Gamma, t),$$

describes the vortex sheet of a two-dimensional inviscid, irrotational flow where Γ is a parameter which measures the circulation between a base point $\Gamma = 0$ and an arbitrary point along the sheet. The vortex-sheet strength $\sigma(\Gamma, t)$ is the jump in tangential velocity across the sheet, i.e.,

$$\sigma(\Gamma, t) = (\mathbf{u}_2 - \mathbf{u}_1) \cdot \mathbf{t},$$

where $\mathbf{t}$ is the vortex sheet tangential vector. The equation governing the motion of the interface is

$$\frac{\partial \bar{z}}{\partial t}(\Gamma, t) = \frac{-i}{2\pi} PV \int_{-\infty}^{\infty} \frac{d\Gamma'}{z(\Gamma, t) - z(\Gamma', t)}, \tag{1.1}$$

$$z(\Gamma, 0) = \Gamma + s(\Gamma, 0). \tag{1.2}$$

where bar over z denotes complex conjugate and PV denotes Cauchy Principal Value. The initial condition (1.2) is a perturbation of the flat vortex sheet of constant strength $z(\Gamma, t) = \Gamma$ and $s(\Gamma, 0)$ is periodic in Γ. Consider a small sinusoidal perturbation to the flat vortex sheet of $z(\Gamma, t) = \Gamma$, i.e.,

$$z(\Gamma, 0) = \Gamma + i\varepsilon \sin \Gamma. \tag{1.3}$$

At later time t, we have

$$z(\Gamma, t) = \Gamma + \sum_{k=-\infty}^{\infty} \hat{A}_k(t)\, e^{ik\Gamma},$$

and analysis of linearized problem shows that

$$\left|\hat{A}_k(t)\right| \sim \varepsilon^{|k|} e^{\frac{\sigma_0 k t}{2}},$$

where σ_0 is the strength or uniform circulation density of the unperturbed vortex sheet. The amplitude $\varepsilon^{|k|}$ comes from the fact that higher order modes are generated from data (1.3) by nonlinear interactions, so that the modes of wavenumber k will have a leading order amplitude of $\varepsilon^{|k|}$. As Moore [28] points out, to examine singularity formation in the linearized problem, it is instructive to consider the analytic continuation. Hence, consider $\Gamma = \Gamma_r + i\Gamma_i$. For positive k, $s(\Gamma, t)$ is an upper analytic function (i.e., analytic in the upper half plane) and there is a singularity in the lower complex plane when the exponential decay of $\left|\hat{A}_k(t)\right|$ is balanced by exponential growth of $e^{-k\Gamma_i}$ ($\Gamma_i < 0$). This balance occurs when

$$-\Gamma_i + \ln \varepsilon + \frac{\sigma_0}{2} t = 0. \tag{1.4}$$

Note that according to (1.4), the singularity moves in the positive imaginary Γ direction and with speed $\frac{\sigma_0}{2}$ reaches the real Γ line at time $t = \frac{2}{\sigma_0}(\Gamma_i - \ln \varepsilon)$ at which point a singularity appears of the interface (in linear theory). Singularity formation in the full nonlinear problem (1.1) has been investigated numerically. Complex singularities are detected by exploiting the relation between the complex singularities of $s(\Gamma, t) = z(\Gamma, t) - \Gamma$ and the asymptotic behavior of its Fourier coefficients [12], [41], and [22]. Suppose $s(\Gamma, t)$ has a singularity at $\Gamma^* = x^* - i\delta(t)$ at which point the local behavior of $s(\Gamma, t)$ is given by

$$s(\Gamma, t) \sim (\Gamma - \Gamma^*)^{\beta}. \tag{1.5}$$

Then the Fourier coefficients of $s(\Gamma, t)$ decay as

$$|\hat{s}_k| \sim k^{-(\beta+1)} e^{-k\delta}, \tag{1.6}$$

in the limit $k \to \infty$. In the Kelvin-Helmholtz problem, the value of $\beta \sim \frac{3}{2}$ is noted analytically by Moore [27], and numerically by Meiron et al. [26] Shelley [39] and Krasny [22].

To obtain the numerical solution for the nonlinear evolution of the vortex sheet, one needs to solve the initial value problem obtained by the point vortex approximation. Previous numerical studies before Krasny [22] had experienced difficulties in converging when the mesh was refined. The results by Krasny indicate the formation of a singularity in the vortex sheet at a finite time. To be more specific, Kelvin-Helmholtz instability has been shown to lead to a development of curvature singularities [28], [27], and [26]. The point vortex approximation converges up to but not beyond the time of singularity formation in the vortex sheet.

Formation of curvature singularities can also occur in the case for Rayleigh-Taylor instability. The classical example of Rayleigh-Taylor instability occurs when a heavy fluid lies above a lighter in the presence of gravity in the case when both fluids are inviscid and irrotational. When the fluids are immiscible, a sharp interface exists between them which deforms into a pattern containing rising bubbles of lighter fluid and falling spikes of heavier fluid. A strong shearing flow develops on the sides of the spikes as the lighter and heavier fluid pass by each other. This part of the interface is then subject to Kelvin-Helmholtz instability. Based on a vortex sheet representation, a set of evolution equations for the location of the interface has been derived by Baker, Meiron, and Orszag (1982) [3], and Moore (1982) [29]. For periodic disturbances from a flat sheet, there is strong evidence that the sheet develops curvature singularities in finite time. Studies by Baker, Caflisch, and Siegel (1993) [1] show how singularities in the complex plane move towards and reach the real axis in finite time, at which point a curvature singularity is observed physically. They track singularities numerically using a more general version of (1.6) in the case where two symmetric singularities are directed to the real line.

In all the above problems, to evolve the interface beyond the singularity time, one needs to employ some form of regularization to avoid numerical difficulties. The regularization prevents the singularities in the complex plane from reaching the real axis. Examples of regularization are vortex blob (Chorin 1973) [13], and (Krasny 1986) [21] vortex patch (Baker and Shelly 1990) [4], and regularization with surface tension (Hou et al. 1994) [18], [17]. Regularization enables one to proceed beyond the singularity time.

As another example let us consider Hele-Shaw flow [37], where we have two parallel plates with a narrow gap between them. Then a less viscous fluid (for example water) is injected into a more viscous fluid (say glycerin). Howison [19] shows that the motion of the interface is ill-posed and small deviations in the initial condition

will produce significant changes in the ensuing motion. As in Kelvin-Helholtz, the problem is ill-posed on linear theory. Howison [19], and Howison et al. [20] also shows that the *nonlinear* problem is ill-posed. He constructs exact solutions using a conformal map $z(\zeta, t)$ which maps the unit disk to fluid region. Howison finds exact solutions in $z(\zeta, t)$ which contains singularities in $|\zeta| > 1$ that move onto $|\zeta| = 1$ at finite time. These solutions are used to demonstrate ill-posedness of the full nonlinear problem.

In this thesis, we use complex variable theory to trace complex singularities. Complex variable theory has been employed extensively in fluid dynamics and partial differential equations. When the complex variables techniques are applicable, they provide strong and useful tools in studying fluid dynamics and PDEs. One of the main method of detecting singular solutions is to extend the computed solution into the complex plane and then analyze the decay of Fourier coefficients using the numerical form fit (1.6) to ascertain the nature of singularities. As we discussed, analyzing the decay of Fourier coefficients using the numerical form fit (1.6) has been successfully applied to study singularity formation in Kelvin-Helmholtz and Rayleigh-Taylor problem.

Asymptotic relations (1.6) and (1.5) have been established for functions of single spatial variable $f(z, t)$ [12], [41]. However, (1.6) has not been extended to higher dimensions. There are ways to use the 1D asymptotic result (1.6) for multidimensional spatial functions. One way is to Fourier transform $f(x, y, z)$ in one variable, say z, with fixed x and y, then analyze the decay of $\hat{f}_k(x, y)$ (i.e., the Fourier coefficients of e^{ikz}) as a function of x and y using (1.6). Another way to use (1.6) for multi-dimensional functions is to take a direction in the multidimensional array of Fourier coefficients. For example one can take the main diagonal, i.e., $\hat{f}_{(k,k)}$ in a two-dimensional matrix of Fourier coefficients $\hat{f}_{(k,l)}$ and then employ (1.6) to analyze singularity [42], [32], and [33]. Pauls et al. [35] have taken such an approach in

analyzing the complex singular solution to 2D-Euler equations. One disadvantage of using above methods is that they miss on some of the qualitative behavior of the higher dimensional singular surfaces as we point out in next Chapters. In addition, in the above methods only small part of the Fourier coefficients are being used and a good deal of the information is lost. In this thesis, we present a new method to detect asymptotic behavior of a two or three-dimensional array of Fourier coefficients to analyze the location and geometry of a singular surface in two and three-dimensions. Note that in 1D complex singularities are points in C, in 2D they are curves in C^2 and in 3D complex singularities are surfaces in C^3.

By analyzing the rate of the decay of the full two and three-dimension of Fourier coefficients, we are able to characterize the singular surfaces. The analytical structure of the solutions in complex plane may aid in the understanding of formation of singularities and may indicate the generic form of singularities. For example, Bessis and Fournier [7], have studied inviscid Burger's equation and showed that the solution has branch point singularities that move in the complex plane. The shock is formed when these singularities reach the real axis. Also, the tracing of singularity in the complex x-domain was reported by Senouf et al. [38], with reference to the viscous and dispersive Burgers equations. We come back to the example of Burger's equation in Chapter 2. In another example, Weidman [43] showed that the blow up in,

$$u_t - \nu u_{xx} + (H(u)u)_x = 0,$$

where ν is a positive constant and H is the Hilbert transform, can be explained by complex poles moving onto the real axis.

To close this Chapter, we discuss a famous and fundamental problem, the Euler singularity problem and its possible connection to complex singularities.

1.2 Euler Singularity Problem

A fundamental question about any differential equation is whether it is well-posed or not. The well-posedness of a differential equation means the existence and uniqueness of the solution plus continuous dependence of the solution on initial and boundary values. For the 3D Euler equations, well-posedness has been answered only partially. Precisely, we have the following outstanding unsolved problem:

Does there exist smooth initial data $\mathbf{u}_0 \in H^s$, with $s \geq 3$ in all of space or with periodic boundary conditions such that the maximum interval of existence of a smooth solution $\mathbf{u}(\mathbf{x},t)$ is finite? That is, is there finite time T^* where $\mathbf{u}(\mathbf{x},T^*) \notin H^s$[6] ? Alternatively, we can ask whether the solution for analytic data $\mathbf{u}_0$ remains so for all time. The main analytical results regarding existence and regularity of the 3D Euler equations is of Beale-Kato-Majda [6] which may be stated roughly as following,

The time interval $[0, T^*)$ with $T^* < \infty$ is a maximal interval of smooth H^s $(s > 5/2)$ existence for the 3D Euler equations if and only if

$$\lim_{t \to T^*} \int_0^t \|\omega\|_{L^\infty}(s)ds = \infty. \tag{1.7}$$

Roughly speaking, the Beale, Kato Majda (BKM) theorem states that if a solution to the Euler equations loose any smoothness, then the vorticity or first derivatives in the velocity must blow up. Furthermore, the maximum vorticity must grow at least like $\frac{1}{T^*-t}$ for singularity formation. Analytical approaches to the Euler singularity problem have been proved to be very difficult; therefore, considerable efforts have been devoted to numerical approaches. All of the numerical efforts for the Euler singularity problem have been inconclusive so far. To detect a potential singularity, one needs to systematically monitor mathematical conditions including the Beale-Kato-Majda theorem or equivalent theorems [44], [14]. Again for this famous open problem, tracing complex singularities might help us in the understanding

of formation of singularities and may indicate the generic form of singularities of Euler equations. As an example, we mention Caflisch [9], and Caflisch and Siegel [11] who calculated the complex singular solutions of Euler equations numerically.

The Euler singularity problem can also be related to turbulence. There is evidence that suggests that Euler singularities play an important role in fluid dynamic turbulence [10] which we now describe. The cornerstone of turbulence theory is the Kolmogorov theory [23] which is based on dimensional analysis and proposes the existence of universal scaling behavior in fully developed turbulence. For example, the Kolmogorov theory predicts that average energy dissipation rate per unit mass, denoted by ε, is bounded above zero [16], i.e., there is a positive constant c such that

$$0 < c \leq \varepsilon \quad \text{as} \quad \nu \to 0, \tag{1.8}$$

it can be shown that

$$\varepsilon = L^{-3}\nu \left\langle \|\nabla \mathbf{u}\|_{L^2}^2 \right\rangle, \tag{1.9}$$

where $\|\cdot\|_2$ is the L^2 *norm* on R^3, L is the scale of the large eddies, and $\langle . \rangle$ is ensemble average which means the average over many experiments under identical set of experimental conditions. There is numerical and experimental evidence that ε is bounded above zero for vanishing ν consistent with Kolmogorov theory. Taken together, (1.8) and (1.9) suggest that $\nabla \mathbf{u}$ approaches infinity as $\nu \to 0$, which is indicative of blow up in the Euler equations. The Euler singularities connect the Kolmogorov theory to the zero viscosity Navier-Stokes dynamics.

The rest of this thesis is organized as follows. In Chapter 2, we discuss asymptotic behavior of 1D Fourier coefficients and give examples of numerical form fit in 1D. In Chapter 3, 1D results are generalized to higher dimensions and a numerical form fit for

detecting singular surface is presented. In Chapter 4, numerical fitting procedure is validated using synthetic data examples. Finally, in Chapter 5, our numerical from fit for detecting singular surface is employed to detect complex singularities of Burger's equation. At the end of Chapter 5, some concluding remarks and suggestions for future work are presented.

CHAPTER 2

NUMERICAL FORM FIT IN 1D

2.1 Asymptotic Behavior of 1D Fourier Coefficients

In this section, we show the asymptotic relation between local singular behavior of a complex function of one variable and its Fourier coefficients.

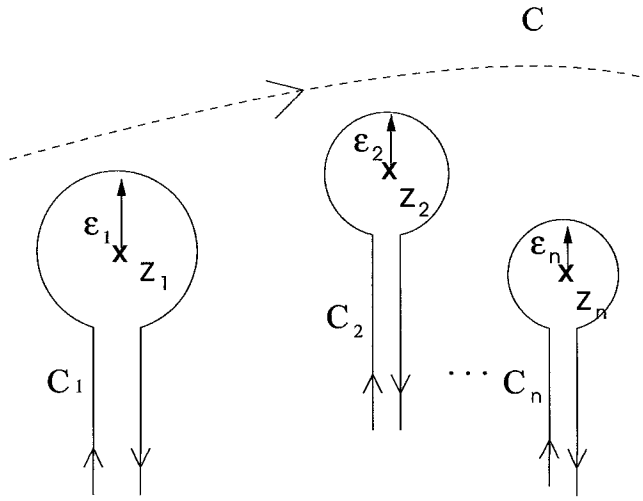

Figure 2.1 Illustration of original integration contour C and deformed contour $\cup_{j=1}^{n} C_j$.

Consider an upper analytic function $f(z)$ (i.e., analytic in upper half plane) with singularities at $z = z_j$, $j = 1, ..., n$, in a neighborhood of which $f(z)$ behaves as,

$$f(z) \sim (z - z_j)^{\beta}, \tag{2.1}$$

where $\beta > -1$. Following [12], we calculate the Fourier integral by contour deformation. Define the Fourier integral

$$I(k) = \int_C e^{-ikz} f(z) dz = \bigcup_{j=1}^{n} I_j(k), \tag{2.2}$$

where the original contour C and deformed contour $\bigcup_{j=1}^{n} C_j$ is illustrated in Figure 2.1, and I_j is the contribution to $I(k)$ from the integral over C_j. The leading order contribution to the integral over C_j is given by

$$I_j(k) \sim \int_{C_j} e^{-ikz}(z - z_j)^{\beta} dz.$$

Set $z - z_j = re^{i\theta}$ where $\frac{-\pi}{2} < \theta \leq \frac{3\pi}{2}$. Then

$$I_j(k) \sim \int_{\infty}^{0} e^{-ik(z_j + re^{i\frac{3\pi}{2}})} r^{\beta} e^{i\frac{3\pi\beta}{2}} e^{i\frac{3\pi}{2}} dr + \int_{0}^{\infty} e^{-ik(z_j + re^{-i\frac{\pi}{2}})} r^{\beta} e^{-i\frac{\pi\beta}{2}} e^{-i\frac{\pi}{2}} dr, \tag{2.3}$$

where on C_{ε_j}, $z - z_j = \varepsilon e^{i\theta}$ for $\frac{-\pi}{2} < \theta \leq \frac{3\pi}{2}$. We have

$$\left| \int_{C_{\varepsilon_j}} e^{-ikz}(z - z_j)^{\beta} dz \right| \leq \varepsilon^{\beta} \int_{-\frac{\pi}{2}}^{\frac{3\pi}{2}} \varepsilon d\theta \to 0 \qquad \text{as} \qquad \varepsilon \to 0,$$

hence the integral around the circular part of C_j, i.e., C_{ε_j}tends to zero as $\varepsilon \to 0$. After simplifying, (2.3) becomes

$$I_j(k) \sim -e^{-ikz_j} e^{-i\frac{\pi\beta}{2}} \left(\frac{e^{i\pi\beta} - e^{-i\pi\beta}}{i}\right) \int_{0}^{\infty} e^{-kr} r^{\beta} dr \sim (-2\sin\pi\beta) e^{-i(kz_j + \frac{\pi\beta}{2})} \int_{0}^{\infty} e^{-kr} r^{\beta} dr,$$

for large k. Employing Watson's lemma, i.e.,

$$\int_{0}^{\infty} e^{-kr} r^{\beta} dr \sim \frac{\Gamma(\beta + 1)}{k^{(\beta+1)}},$$

where $\Gamma(z)$ is the Gamma function. We obtain,

$$I_j(k) \sim (-2\sin\pi\beta)(e^{-i\frac{\pi\beta}{2}})\Gamma(\beta + 1) e^{-ikz_j} k^{-(\beta+1)}, \tag{2.4}$$

at leading order for $k >> 1$.

When the asymptotic contributions from the other z_j are added, so as to give an asymptotic expression for $I(k)$ itself, the behavior of $I(k)$, for large k, is dominated by the particular $I_j(k)$ associated with the z_j of largest imaginary part (for functions in the upper half-plane this z_j is closest singularity to the real axis). If this singularity is located at $z_j^* = x^* - i\delta$, $\delta > 0$ then by (2.4)

$$\hat{f}_k \sim C(\beta)k^{-(\beta+1)}e^{-k\delta}e^{-ikx^*} \qquad \text{as } k \to \infty, \tag{2.5}$$

where $C(\beta) = (-2\sin\pi\beta)(e^{-i\frac{\pi\beta}{2}})\Gamma(\beta+1)$. From (2.5)

$$\ln\left|\hat{f}_k\right| = \ln|C(\beta)| - (\beta+1)\ln k - k\delta. \tag{2.6}$$

Following [22] $C(\beta)$, β and δ are numerically determined by a sliding fit. We implement a three parameter fit using (2.6) which gives the following nonsingular system of equations

$$\begin{pmatrix} \ln\left|\hat{f}_k\right| \\ \ln\left|\hat{f}_{k+1}\right| \\ \ln\left|\hat{f}_{k+2}\right| \end{pmatrix} = \begin{pmatrix} 1 & -\ln|k| & -k \\ 1 & -\ln|k+1| & -(k+1) \\ 1 & -\ln|k+2| & -(k+2) \end{pmatrix} \begin{pmatrix} \ln|C(\beta)| \\ \beta+1 \\ \delta \end{pmatrix}. \tag{2.7}$$

Note that an alternative way to obtains $C(\beta)$, β, and δ is least square method employed by Sulem et al [41].

To see (2.1), (2.5) and (2.7) in action, we present a synthetic example

$$f(x) = \frac{1}{\sqrt{1-\varepsilon e^{ix}}}, \tag{2.8}$$

where for illustration we use $\varepsilon = 0.9$. Comparing (2.8) and (2.1) gives $\beta = -\frac{1}{2}$ and $\delta = \ln(\frac{10}{9})$. Figure 2.2 compares numerical form fit for β and δ with their actual

values. The figure shows that the fits accurately detect the distance of the singularity from the real line δ, and the singularity exponent β.

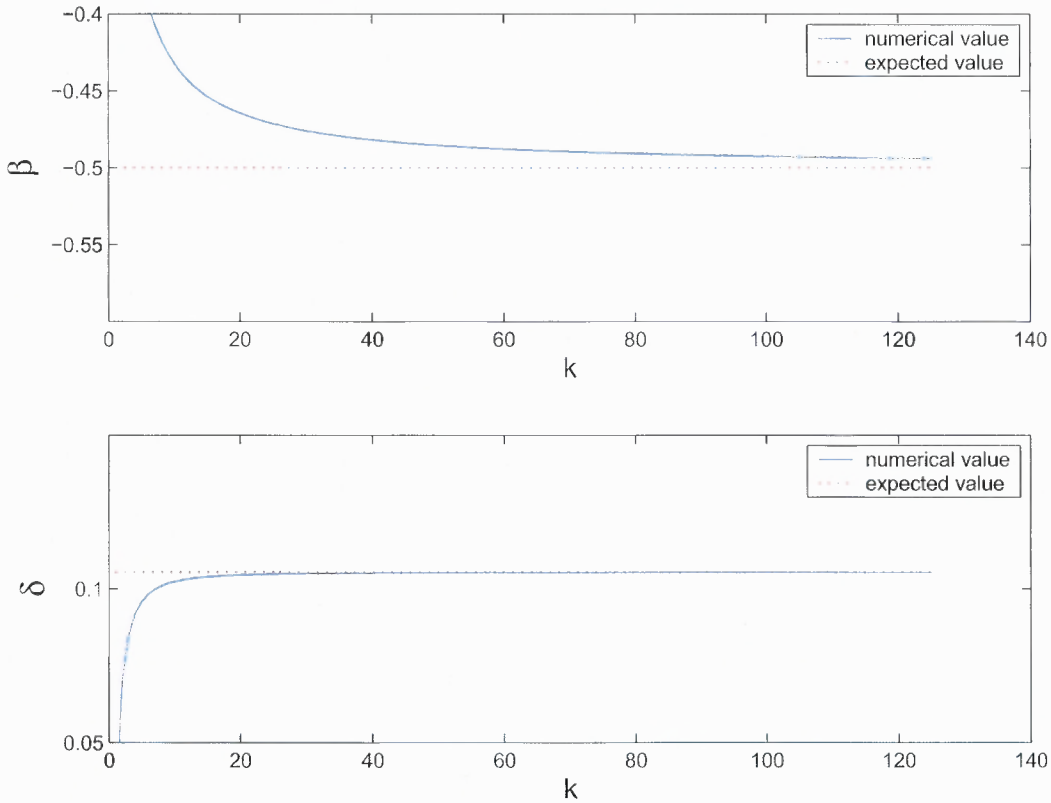

Figure 2.2 Sliding fit of $\beta(k)$ and $\delta(k)$ using (2.7) plotted versus k. The solid line gives the numerically calculated values of β and δ while the red dotted line gives the actual values.

In the next section, we present examples of the application of (2.5) and (2.7) in computing singular solutions of inviscid Burger's equation plus we mention some alternative methods.

2.2 Canonical Example: Singular Solution of Inviscid Burger's Equation

In Cartesian coordinate the inviscid Burger's equation is given by,

$$u_t + uu_x = 0, \qquad u(x,0) = f(x), \tag{2.9}$$

where we assume $u(x,t)$ is periodic in x. The inviscid Burger's equation, among other phenomenon describes the flow caused by a dam break. The left hand side of (2.9) is the total derivative of u along a characteristic $x(t,x_0)$ emanating from x_0, with equation $\frac{dx}{dt} = u$. Hence

$$\frac{du}{dt} = 0 \qquad \text{and} \qquad u(0) = f(x_0),$$

along the characteristic

$$\frac{dx}{dt} = u, \qquad x(0) = x_0,$$

so that

$$x = ut + x_0. \tag{2.10}$$

Hence the implicit solution to (2.9) is given by,

$$u(x,t) = f(x - ut).$$

As an example, we consider the case in (2.9) where $f(x) = -\sin x$, i.e., $u(x,t)$ is periodic in x and

$$u_t + uu_x = 0, \qquad u(x,0) = -\sin x, \tag{2.11}$$

the solution to (2.11) develops shocks which appears at $t = 1$ at $x = 0$. It has been analytically shown that [41] at time $t = 0^+$, a conjugate pair of complex singularities are formed on the imaginary axis with local behavior

$$u(z,t) \sim (z - z'(t))^{\frac{1}{2}} \qquad t < 1, \tag{2.12}$$

$$u(x,t) \sim (x - x')^{\frac{1}{3}} \qquad t = 1, x' = 0, \tag{2.13}$$

where z' is a complex singularity location for $t < 1$, z is a complex variable while x is a real variable, and x' is real singularity location for $t = 1$ and from (2.12) and (2.13), we conclude that the analytical continuation of the real solution to the complex plane develops square root singularities on the imaginary axis before time $t = 1$. Then at $t = 1$, the complex singularities reach the real axis. The two singularities then collide to form a single cube root singularity. To investigate this numerically, we consider the large wavenumber behavior of the numerical solution in Fourier space, i.e., we employ (2.5) for large k and then solve (2.7) to obtain β and δ.

To find the numerical solution of (2.11), we apply a pseudospectral method. In this approach, we use leap frog formula for the time derivatives and approximate the spatial derivatives spectrally, using the FFT. The leap-frog scheme requires two initial conditions to start with, whereas the PDE (2.11) provides only one. To obtain another starting value, second order Runge-Kutta formula has been employed. In Figure 2.3, the top is the plot of u versus (x,t) at equally space time between t=0 and t=1. The bottom is the $\log_{10}|\hat{u}_k|$ versus k at equally space time berween t=0.25 and t=1. Note that as it gets closer to the singularity formation time $t = 1$, the spectrum is becoming flatter. Figure 2.4 illustrates plots of the sliding form fit for β and δ at t=0.9 and t=1.

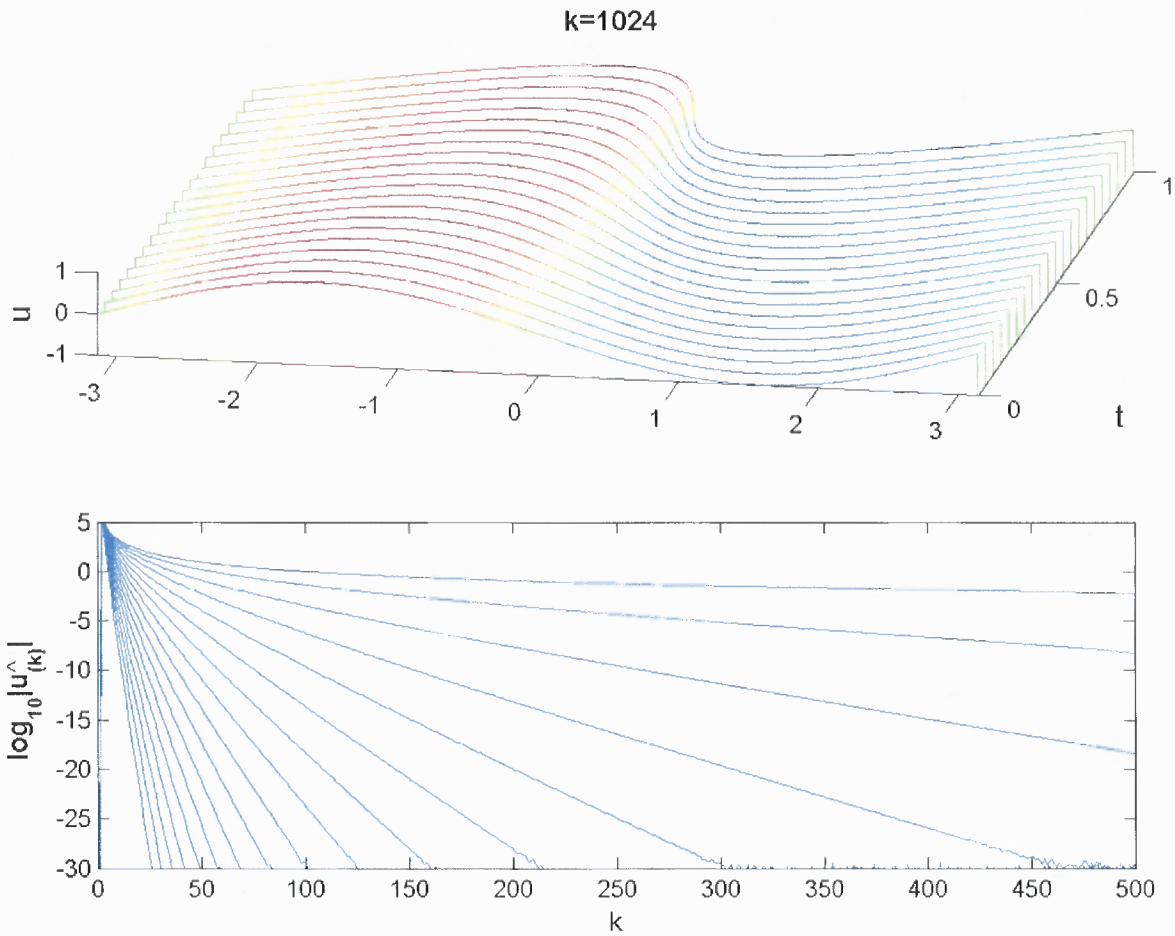

Figure 2.3 The top is the numerical solution of inviscid Burger's equation at a equally space time between $t = 0$ and $t = 1$ in steps of 0.05 with time shown on axis at right. The solution develops shock at $t = 1$. The bottom is the Fourier transform of the linear-log scale (i.e., $\log|\hat{u}_k|$ versus k) at equally spaced time between $t = 0.25$ and $t = 1$ in steps of 0.05.

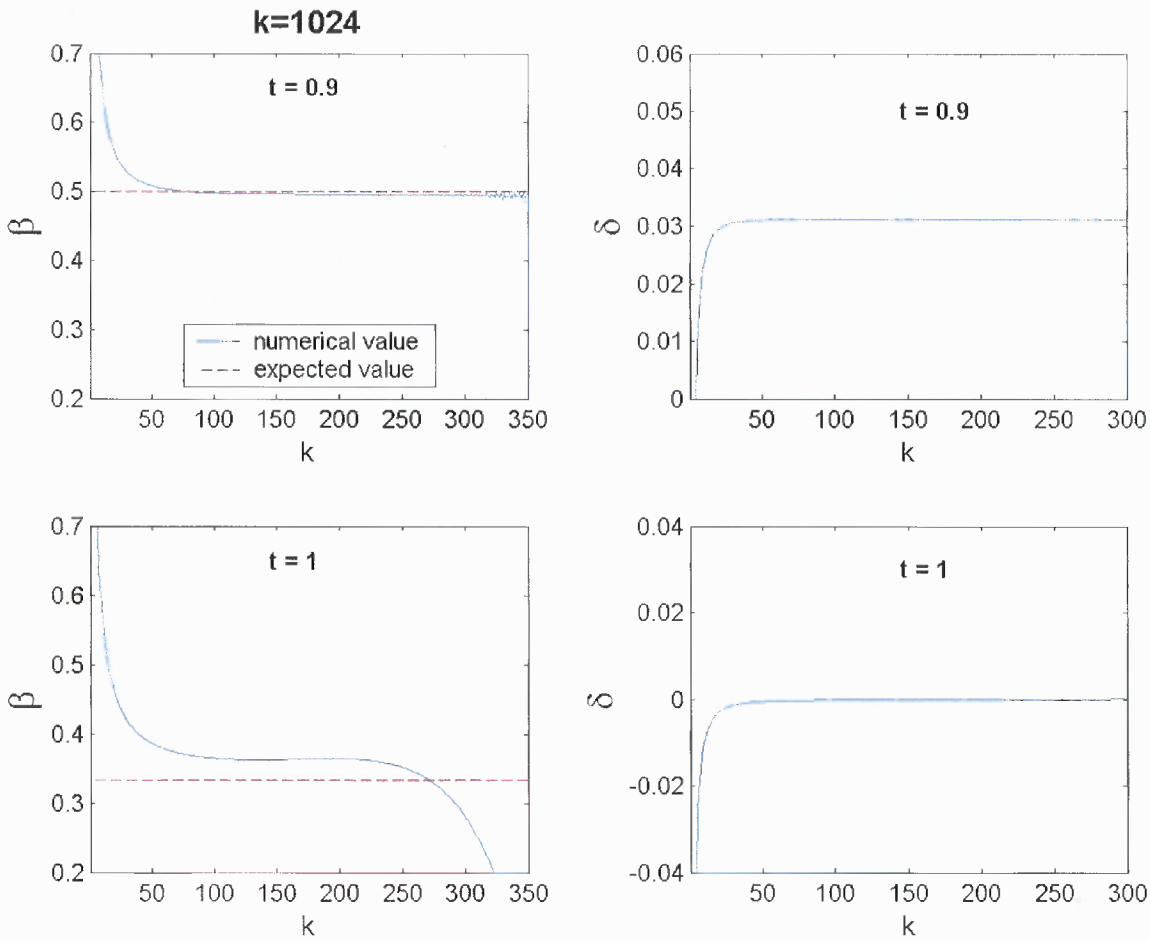

Figure 2.4 Plots of sliding fit for $\beta(k)$ (solid blue curve) compared with their values (red dashed line), and plots of $\delta(k)$ on the right side. At $t = 0.9$, $\beta \sim \frac{1}{2}$ and $\delta \sim 0.03$ while at the shock formation time, i.e., $t = 1$, $\beta \sim \frac{1}{3}$ and $\delta \sim 0$ which is what we expect.

We have been able to obtain information on the nature and location of the singularities by examining the rate of decay of Fourier coefficients. It is worth noting that there are alternative approaches to detect complex singularity. Weideman [43] utilizes the Padé approximation to gain information on the nature and location of the singularities of

$$u_t + uu_x = 0, \qquad u(x,0) = e^{ix}. \tag{2.14}$$

In the following we give a brief introduction to his approach. For a function such as

$$f(z) = \sum_{k=0}^{\infty} c_k z^k,$$

the $[L, M]$ Padé approximation, is defined as the rational function

$$[L/M] = \frac{a_0 + a_1 z + \cdots + a_L z^L}{1 + b_1 z + \cdots + b_m z^m}, \tag{2.15}$$

with the property that

$$f(z) - [L/M] = O\left(z^{L+M+1}\right).$$

In terms of Fourier series, assume

$$u(z) \sim \sum_{n=-N}^{n=N} a_n e^{inz},$$

truncated at $2N+1$ terms. When $z = x$ is real, this would be an approximate solution to a PDE such as (2.9) at a specific time t. By defining $w = e^{iz}$ and $v = e^{-iz}$, the Fourier series on the right may be expressed as

$$u(z) \sim \sum_{n=0}^{N} a_n w^n + \sum_{n=0}^{N} a_{-n} v^n - a_0. \tag{2.16}$$

Both power series on the right can be converted to Padé approximations of the form (2.15). To locate the pole, Weideman applies a numerical maximization search to the objective function $f(z) = \log|u(z)|$. To compute the order of the pole, he employs the principle of the argument [12]. Weideman compares the numerical

detection of complex singularities using Padé approximations to an exact solution for periodic Burger's equation [12] given by

$$u = (\frac{1}{it})W(ite^{ix}),$$

where $w = W(z)$ solves the equation $we^w = z$, i.e., $W(z)$ is the Lambert function.

He also gives two more examples of employing Padé approximation to locate and characterize the singularities of PDEs. His first example is nonlinear heat equation

$$u_t - u_{xx} - u^2 = 0, \qquad u(x,0) = \cos x,$$

and the second example is

$$u_t - \nu u_{xx} + (H(u)u)_x = 0,$$

where ν is a positive constant and H is the Hilbert transform. The exact solution for the latter PDE is [2]

$$u(x,t) = \sigma + \nu \frac{1 - \rho^2 e^{2\sigma t}}{1 + \rho^2 e^{2\sigma t} - 2\rho e^{\sigma t} \cos x}$$

and therefore the initial condition is $u\,(x,0)$ i.e.

$$u\,(x,0) = \sigma + \nu \frac{1 - \rho^2}{1 + \rho^2 - 2\rho \cos x}$$

with σ and ρ are arbitrary positive constants.

Another analysis of complex singularity for Burger's equation is given by Platzman [36] and Muraki [30]. Platzman finds a Fourier series solution of (2.9) although, at

first glance, it seems that the nonlinearity of (2.9) precludes the usual application of Fourier transform. He assumes

$$u(x,t) = \frac{a_0}{2} + \sum_{n=1}^{\infty}[a_n(t)\cos nx + b_n(t)\sin nx], \tag{2.17}$$

$$a_n(t) = \frac{1}{\pi}\int_{-\pi}^{\pi} u(x,t)\cos(nx)dx,$$

$$b_n(t) = \frac{1}{\pi}\int_{-\pi}^{\pi} u(x,t)\sin(nx)dx.$$

For the sine coefficient $b_n(t)$, apply integration by parts, followed by a replacement of u_x using (2.10)

$$b_n(t) = \frac{1}{\pi n}\int_{-\pi}^{\pi} u_x(x,t)\cos(nx)dx,$$

$$= \frac{1}{\pi nt}\int_{-\pi}^{\pi}(1 - \frac{dx_0}{dx})\cos(nx)dx.$$

Changing the variable of integration to x_0 gives

$$b_n(t) = -\frac{1}{\pi nt}\int_{-\pi}^{\pi}\cos[nx_0 + ntf(x_0)]dx_0 \tag{2.18}$$

which only depends on initial condition $u(x,0) = f(x_0)$. Note that the use of integration by parts assumes that the solution (and its spatial derivative, i.e., u_x) remains continuous, and hence is not valid after the shock formation. The same way, one can obtain the cosine coefficients

$$a_n(t) = \frac{1}{\pi n t} \int_{-\pi}^{\pi} \sin[n x_0 + n t f(x_0)] dx_0 \qquad \text{for } n > 0, \tag{2.19}$$

and

$$a_0 = \frac{1}{\pi} \int_{-\pi}^{\pi} f(x_0) dx_0. \tag{2.20}$$

Substituting the Fourier coefficients (2.20), (2.19), and (2.18) back into (2.17) leads to

$$u(x,t) = \frac{a_0}{2} + \sum_{n=1}^{\infty} \frac{1}{\pi n t} \int_{-\pi}^{\pi} \sin[n(x - x_0 - t f(x_0))] dx_0. \tag{2.21}$$

For the case when the initial condition is $u(x,0) = -\sin x$, i.e., (2.11), the Fourier coefficients (2.18) becomes

$$b_n(t) = -\frac{1}{\pi n t} \int_{-\pi}^{\pi} \cos[n x_0 - n t \sin x_0] dx_0 = -2 \frac{J_n(nt)}{nt}, \tag{2.22}$$

when $J_n(nt)$ is the Bessel function of order n. This generates a Fourier sine series solution to (2.11),

$$u(x,t) = -2 \sum_{n=1}^{\infty} \frac{J_n(nt)}{nt} \sin nx.$$

In addition, one can expand (2.22) asymptotically and obtain an explicit formula for the Fourier coefficients [30]

$$|b_n| \sim \sqrt{\frac{2}{\pi t^2 \tanh \alpha}} n^{\frac{-3}{2}} e^{n(-\alpha + \tanh \alpha)}, \tag{2.23}$$

as $n \to \infty$, where $\cosh \alpha = \frac{1}{t}$. The asymptotic formula (2.23) implies there is a square root singularity ($\beta = \frac{1}{2}$) located a distance ($\alpha - \tanh \alpha$) from real line. The above expansion of Fourier coefficient $|b_n(t)|$ is equivalent with (2.12).

As we mention before, relations (2.5) has not been extended to functions of two or three values. In the next Chapter, we present a new method to extend (2.5) to higher dimensions.

CHAPTER 3

DETECTING A SINGULAR SURFACE IN 2D AND 3D

3.1 Introduction

In Chapter 2, we have shown that if $u(z)$ is an analytic function with singularities located in the lower complex plane at z_j, in a neighborhood of which it behaves as,

$$u(z) \sim (z - z_j^*)^\beta, \tag{3.1}$$

then the behavior of the Fourier transform of $u(z)$ for large k is governed by the singularity closest to the real axis. If this singularity is located at

$$z_j^* = \delta_R^* - i\delta_I^* \qquad \text{where} \qquad \delta_i^* > 0 \tag{3.2}$$

then

$$\hat{u}_k \sim C(\beta)k^{-(\beta+1)}e^{-k\delta_R^*}e^{-ik\delta_I^*} \quad as \quad k \to \infty. \tag{3.3}$$

where $C(\beta)$ and β are complex.

In this Chapter, following ideas of Caflisch [8], we present a new method to detect asymptotic behavior of a two or three-dimensional array of Fourier coefficients to analyze the location and geometry of singular surface in two and three dimensions. Also, we remind the readers that in $1D$ complex singularities are points in C, in $2D$ they are curves in C^2 and in $3D$ complex singularities are surfaces in C^3.

Consider a function $u(x, y, z) : R^3 \to C$, which is 2π periodic in x, y and z. To motivate the extension of (3.3) for multidimensional functions such as $u(x, y, z)$, it is helpful to consider the analytic continuation of $u(x, y, z)$ in a single variable, e.g., x, with the other two variables taken as real parameters. Assume $u(x, y, z)$ is analytic for x in a strip in C given by

$$|Imx| < \rho, \qquad \text{for some } \rho > 0.$$

The function $u(x, y, z)$ has a Fourier series representation, which we write as

$$u = \sum_{k=-\infty}^{k=\infty} \hat{u}_k(y, z) e^{ikx}$$

denote $u_+ = \sum_{k>0} \hat{u}_k(y, z) e^{ikx}, u_- = \sum_{k<0} \hat{u}_k(y, z) e^{ikx}$ and $u_0 = \hat{u}_0$. The function u_+ is *upper analytic*, i.e., analytic for Im $x > -\rho$. Similarly, u_- is *lower analytic, i.e.,* analytic in Im $x < \rho$. Motivated by $1D$ discussion, we expect $u_+(x, y, z)$ to have singularities in the lower half-plane at $x_0 = x_0(y, z)$ where

$$x_0(y, z) = \delta_R(y, z) - i\delta_I(y, z), \tag{3.4}$$

and $\delta_I(y, z) > 0$.

The closest singularity to the real line is that which minimizes $\delta_I(y, z)$. Assume the closest singularity is located at $(y, z) = (y_0, z_0)$ and that $\delta_I(y, z)$ is smooth in a neighborhood of (y_0, z_0). In the generic case, we expect that $\delta_I(y, z)$ is *paraboloidal* near $(y, z) = (y_0, z_0)$. Let $\mathbf{X}_0 = (x_0, y_0, z_0)$ be the point on the singularity surface that is closest to real (physical) space, then the previous discussion suggests that the singular surface near $\mathbf{X}_0$ is paraboloidal and after a rotation of variables the surface can be described as $\zeta = 0$ with

$$\zeta = x' - \mathbf{A} \cdot \mathbf{Y}' + i\mathbf{Y}' \cdot \mathbf{M}\mathbf{Y}', \tag{3.5}$$

$$x' = x - x_0, \quad \mathbf{Y}' = (y - y_0, z - z_0)^T, \tag{3.6}$$

for $\mathbf{A}$ a real vector and $\mathbf{M}$ a self-adjoint and positive definite 2×2 matrix. This says that there is a singularity at $\mathbf{X}_0$, and that as (y, z) varies away from (y_0, z_0) the imaginary part of the singularity position grows quadratically in the negative direction. The real part of the singularity position is given by $\mathbf{A} \cdot \mathbf{Y}'$ and can vary linearly with y and z.

3.2 Asymptotic Behavior of Multidimensional Fourier Coefficients

Let

$$u = u_0 \zeta^{\beta}, \tag{3.7}$$

where ζ, X', and $\mathbf{Y}'$ are given by (3.5), (3.6) and y_0, z_0 are real.

We follow [8] to compute $\hat{u}_{\mathbf{k}}$ where we denote $\mathbf{k} = (k, l, m)$, $\mathbf{l} = (l, m)$, $\mathbf{X} = (x, y, z)$ and $\mathbf{X}_0 = (x_0, y_0, z_0)$,

$$\hat{u}_{\mathbf{k}} = \iiint\limits_{R^3} u_0(x' - \mathbf{A} \cdot \mathbf{Y}' + i\mathbf{Y}' \cdot \mathbf{M}\mathbf{Y}')^{\beta} \exp(-i\mathbf{k} \cdot \mathbf{X}) dx' \mathbf{d}\mathbf{Y}'.$$

First, perform a shift by (x_0, y_0, z_0) to obtain,

$$\hat{u}_{\mathbf{k}} = u_0 \exp(-i\mathbf{k} \cdot \mathbf{X}_0) \iiint\limits_{R^3} [(x' - \mathbf{A} \cdot \mathbf{Y}' + i\mathbf{Y}' \cdot \mathbf{M}\mathbf{Y}')^{\beta} \exp(-ikx') \exp(-i\mathbf{l} \cdot \mathbf{Y}')] dx' \mathbf{d}\mathbf{Y}',$$

and by using (3.3) for large k,

$$\int\limits_{R} (x' - \mathbf{A} \cdot \mathbf{Y}' + i\mathbf{Y}' \cdot \mathbf{M}\mathbf{Y}')^{\beta} \exp(-ikx') dx' = c_{\beta} k^{-(\beta+1)} \exp(-ik\mathbf{A} \cdot \mathbf{Y}' - k\mathbf{Y}' \cdot \mathbf{M}\mathbf{Y}'),$$

therefore;

$$\hat{u}_{\mathbf{k}} = u_0 \exp(-i\mathbf{k} \cdot \mathbf{X}_0) c_{\beta} k^{-(\beta+1)} \iint\limits_{R^2} \exp(-ik\mathbf{A} \cdot \mathbf{Y}' - k\mathbf{Y}' \cdot \mathbf{M}\mathbf{Y}') \exp(-i\mathbf{l} \cdot \mathbf{Y}') \mathbf{d}\mathbf{Y}'. \tag{3.8}$$

The integral in (3.8) is the Fourier transform of a quadratic exponential and can be computed analytically. We denote that part with I, i.e.,

$$I = \iint_{R^2} \exp(-ik\mathbf{A}\cdot\mathbf{Y}' - k\mathbf{Y}'\cdot\mathbf{M}\mathbf{Y}')\exp(-i\mathbf{l}\cdot\mathbf{Y}')\mathbf{d}\mathbf{Y}'.$$

This integral can be directly calculated. First, since $\mathbf{M}$ is positive definite,

$$\mathbf{M} = \mathbf{U}^T\mathbf{\Lambda}\mathbf{U}, \tag{3.9}$$

where $\mathbf{\Lambda} = diag(\lambda, \mu)$, $\mathbf{U}$ is orthogonal and $\mathbf{U}^T$ is the transpose of $\mathbf{U}$. Let

$$\tilde{\mathbf{Y}} = \mathbf{U}\mathbf{Y}' = (\tilde{y}, \tilde{z})^T,$$

$$\tilde{\mathbf{A}} = \mathbf{U}\mathbf{A}, \quad \tilde{\mathbf{l}} = \mathbf{U}\mathbf{l}, \quad \mathbf{d}\tilde{\mathbf{Y}} = \mathbf{d}\mathbf{Y}',$$

then

$$\mathbf{A}\cdot\mathbf{Y}' = \mathbf{A}^T\mathbf{U}^T\mathbf{U}\mathbf{Y}' = (\mathbf{U}\mathbf{A})^T(\mathbf{U}\mathbf{Y}') = \tilde{\mathbf{A}}\cdot\tilde{\mathbf{Y}} = \tilde{a}\tilde{y} + \tilde{b}\tilde{z},$$

$$\mathbf{l}\cdot\mathbf{Y}' = \mathbf{l}^T\mathbf{U}^T\mathbf{U}\mathbf{Y}' = (\mathbf{U}\mathbf{l})^T(\mathbf{U}\mathbf{Y}') = \tilde{\mathbf{l}}.\tilde{\mathbf{Y}},$$

and

$$\mathbf{Y}'^T\mathbf{M}\mathbf{Y}' = \mathbf{Y}'^T\mathbf{U}^T\mathbf{\Lambda}\mathbf{U}\mathbf{Y}' = (\mathbf{U}\mathbf{Y}')^T\mathbf{\Lambda}(\mathbf{U}\mathbf{Y}') = \tilde{\mathbf{Y}}^T\mathbf{\Lambda}\tilde{\mathbf{Y}} = \lambda\tilde{y}^2 + \mu\tilde{z}^2.$$

Therefore, we can calculate the exponent in the integral I, i.e.,

$$-k\mathbf{Y}'\cdot\mathbf{M}\mathbf{Y}' - ik\mathbf{A}\cdot\mathbf{Y}' - i\mathbf{l}\cdot\mathbf{Y}' = -k(\lambda\tilde{y}^2 + \mu\tilde{z}^2) - ik(\tilde{a}\tilde{y} + \tilde{b}\tilde{z}) - i(\tilde{l}\tilde{y} + \tilde{m}\tilde{z}), \tag{3.10}$$

now by completing the square on the right side of equation (3.10),

$$-k\mathbf{Y}'\cdot\mathbf{M}\mathbf{Y}' - ik\mathbf{A}\cdot\mathbf{Y}' - i\mathbf{l}\cdot\mathbf{Y}'$$

$$= -k\lambda(\tilde{y} + i(\frac{k\tilde{a} + \tilde{l}}{2k\lambda}))^2 - \frac{(k\tilde{a} + \tilde{l})^2}{4k\lambda} - k\mu(\tilde{z} + i(\frac{k\tilde{b} + \tilde{m}}{2k\mu}))^2 - \frac{(k\tilde{b} + \tilde{m})}{4k\mu}, \tag{3.11}$$

which implies

$$I = \iint_{R^2} \exp[-k\lambda(\tilde{y} + i(\frac{k\tilde{a} + \tilde{l}}{2k\lambda}))^2 - \frac{(k\tilde{a} + \tilde{l})^2}{4k\lambda} - k\mu(\tilde{z} + i(\frac{k\tilde{b} + \tilde{m}}{2k\mu}))^2 - \frac{(k\tilde{b} + \tilde{m})}{4k\mu}]d\tilde{y}d\tilde{z}. \tag{3.12}$$

By contour deformation of a standard quadratic integral it is seen that

$$\int_{-\infty}^{\infty} \exp[-k\lambda(\tilde{y} + i(\frac{k\tilde{a} + \tilde{l}}{2k\lambda}))^2]d\tilde{y} = \sqrt{\frac{\pi}{k\lambda}},$$

and

$$\int_{-\infty}^{\infty} \exp[-k\mu(\tilde{z} + i(\frac{k\tilde{b} + \tilde{m}}{2k\mu}))^2]d\tilde{z} = \sqrt{\frac{\pi}{k\mu}}.$$

Therefore,

$$I = \frac{\pi}{k\sqrt{\det(\mathbf{M})}} \exp(-\frac{(k\tilde{a} + \tilde{l})^2}{4k\lambda} - \frac{(k\tilde{b} + \tilde{m})^2}{4k\mu}).$$

Also,

$$-\frac{(k\tilde{a} + \tilde{l})^2}{4k\lambda} - \frac{(k\tilde{b} + \tilde{m})^2}{4k\mu} = \frac{-1}{4k}(k\tilde{\mathbf{A}} + \tilde{\mathbf{l}})^T \mathbf{\Lambda}^{-1}(k\tilde{\mathbf{A}} + \tilde{\mathbf{l}}) = \frac{-1}{4k}(k\mathbf{A} + \mathbf{l})^T \mathbf{M}^{-1}(k\mathbf{A} + \mathbf{l}).$$

Hence

$$I = \iint_{R^2} \exp(-ik\mathbf{A} \cdot \mathbf{Y}' - k\mathbf{Y}' \cdot \mathbf{M}\mathbf{Y}') \exp(-i\mathbf{l} \cdot \mathbf{Y}')\mathbf{dY}'$$

$$= \frac{\pi}{k\sqrt{\det(\mathbf{M})}} \exp[\frac{-1}{4k}(k\mathbf{A} + \mathbf{l})^T \mathbf{M}^{-1}(k\mathbf{A} + \mathbf{l})]. \tag{3.13}$$

Substituting (3.13) into (3.8), we have,

$$\hat{u}_{\mathbf{k}} = u_0 \exp(-i\mathbf{k} \cdot \mathbf{X}_0) c_\beta k^{-(\beta+1)} \frac{\pi}{k\sqrt{\det(\mathbf{M})}} \exp[\frac{-1}{4k}(k\mathbf{A} + \mathbf{l})^T \mathbf{M}^{-1}(k\mathbf{A} + \mathbf{l})],$$

or,

$$\hat{u}_{\mathbf{k}} = C_\beta \exp(-i\mathbf{k} \cdot \mathbf{X}_0) k^{-(\beta+2)} \exp[\frac{-1}{4k}(k\mathbf{A} + \mathbf{l})^T \mathbf{M}^{-1}(k\mathbf{A} + \mathbf{l})], \tag{3.14}$$

where

$$C_\beta = u_0 \frac{\pi}{\sqrt{\det(\mathbf{M})}} c_\beta, \qquad \mathbf{X}_0 = (x_0, y_0, z_0).$$

As in 1D case (3.3), assume $x_0 = x^* - i\delta$, $\delta > 0$, i.e., x_0 is the closest singularity is in the lower complex $x-$plane, Hence

$$\hat{u}_{\mathbf{k}} = C_\beta \exp[-i(k(x_* - i\delta) + ly_0 + mz_0)]k^{-(\beta+2)} \exp[-\frac{(k\tilde{a}+l)^2}{4k\lambda} - \frac{(k\tilde{b}+m)^2}{4k\mu}]. \quad (3.15)$$

On the other hand, y_0, z_0 are real; therefore,

$$|\hat{u}_{\mathbf{k}}| = C_\beta \exp(-k\delta)k^{-(\beta+2)} \exp[-\frac{(k\tilde{a}+l)^2}{4k\lambda} - \frac{(k\tilde{b}+m)^2}{4k\mu}],$$

and

$$\ln|\hat{u}_{\mathbf{k}}| = \ln|C_\beta| - (\beta+2)\ln k - (\delta + \frac{\tilde{a}^2}{4\lambda} + \frac{\tilde{b}^2}{4\mu})k - \frac{\tilde{a}l}{2\lambda} - \frac{l^2}{4\lambda k} - \frac{\tilde{b}m}{2\mu} - \frac{m^2}{4k\mu}. \quad (3.16)$$

There are 7 unknowns in (3.16), namely,

$$C_\beta, \delta, \beta, \tilde{a}, \tilde{b}, \lambda, \mu. \quad (3.17)$$

In the next Chapter, a numerical scheme for obtaining $C_\beta, \delta, \beta, \tilde{a}, \tilde{b}, \lambda, \mu$ is discussed.

3.3 Numerical Form Fit for Detecting Singular Surface

For fixed k, $\ln|\hat{u}_{\mathbf{k}}|$ is quadratic polynomial in l, m. Assume

$$\ln|\hat{u}_{\mathbf{k}}| = \ln\left|\hat{u}_{(k,l,m)}\right| = \gamma_0 + \gamma_1 l + \gamma_2 l^2 + \gamma_3 m + \gamma_4 m^2, \quad (3.18)$$

where

$$\gamma_0 = \ln|C_\beta| - \alpha \ln k - (\delta + \frac{\tilde{a}^2}{4\lambda} + \frac{\tilde{b}^2}{4\mu})k, \qquad \alpha = \beta + 2, \quad (3.19)$$

and

$$\gamma_1 = \frac{-\tilde{a}}{2\lambda}, \qquad \gamma_2 = \frac{-1}{4\lambda k}, \qquad \gamma_3 = \frac{-\tilde{b}}{2\mu}, \qquad \gamma_4 = \frac{-1}{4k\mu}. \tag{3.20}$$

Following the 1D case (2.5) and (2.7), we implement a sliding fit method to obtain $\gamma_0, \gamma_1, \gamma_2, \gamma_3$, and γ_4. Applying 5 values of (l, m) in (3.18) gives the following non-singular system of equations

$$\begin{pmatrix} \ln\left|\hat{u}_{(k,l,m)}\right| \\ \ln\left|\hat{u}_{(k,l+1,m)}\right| \\ \ln\left|\hat{u}_{(k,l+2,m)}\right| \\ \ln\left|\hat{u}_{(k,l,m+1)}\right| \\ \ln\left|\hat{u}_{(k,l,m+2)}\right| \end{pmatrix} = \begin{pmatrix} 1 & l & l^2 & m & m^2 \\ 1 & l+1 & (l+1)^2 & m & m^2 \\ 1 & l+2 & (l+2)^2 & m & m^2 \\ 1 & l & l^2 & m+1 & (m+1)^2 \\ 1 & l & l^2 & m+2 & (m+2)^2 \end{pmatrix} \begin{pmatrix} \gamma_0 \\ \gamma_1 \\ \gamma_2 \\ \gamma_3 \\ \gamma_4 \end{pmatrix}. \tag{3.21}$$

By having $\gamma_0, \gamma_1, \gamma_2, \gamma_3, \gamma_4$ one easily acquires $\tilde{a}, \tilde{b}, \lambda, \mu$ since (3.20) leads to

$$\lambda = \frac{-1}{4k\gamma_2}, \qquad \tilde{a} = -2\lambda\gamma_1, \qquad \mu = \frac{-1}{4k\gamma_4}, \qquad \tilde{b} = -2\mu\gamma_3. \tag{3.22}$$

By knowing $\gamma_0, \tilde{a}, \tilde{b}, \lambda, \mu$ and making use of (3.19), one can attain C, δ, β. Precisely, from (3.19)

$$\gamma_0(k) + \frac{\tilde{a}^2}{4\lambda}k + \frac{\tilde{b}^2}{4\mu}k = \ln|C| - \alpha \ln k - \delta k, \tag{3.23}$$

for fixed (l, m). Applying (3.23) for 3 values of k, we have the following non-singular system of equations,

$$\begin{pmatrix} \gamma_0(k) + \frac{\tilde{a}^2}{4\lambda}k + \frac{\tilde{b}^2}{4\mu}k \\ \gamma_0(k+1) + \frac{(k+1)\tilde{a}^2}{4\lambda} + \frac{(k+1)\tilde{b}^2}{4\mu} \\ \gamma_0(k+2) + \frac{(k+2)\tilde{a}^2}{4\lambda} + \frac{(k+2)\tilde{b}^2}{4\mu} \end{pmatrix} = \begin{pmatrix} 1 & -k & -\ln k \\ 1 & -(k+1) & -\ln(k+1) \\ 1 & -(k+2) & -\ln(k+2) \end{pmatrix} \begin{pmatrix} \ln|C| \\ \delta \\ \beta \end{pmatrix}. \tag{3.24}$$

A successful fit to these parameters is achieved when the values are approximately independent of k. In solving systems of equations (3.21) and (3.24), 5 values of (l, m) and 3 values of k have been chosen. Therefore, in this method, we use a three-dimensional block of fifteen elements out of a three-dimensional array of Fourier coefficients $u_{(k,l,m)}$ every time we calculate $C(k), \delta(k), \beta(k)$ for some k. For example, to compute $\beta(1)$ from (3.24), one needs to obtain $\gamma_0(i), \tilde{a}(i), \tilde{b}(i), \lambda(i), \mu(i)$ for $i = 1, 2, 3$. On the other hand, $\hat{u}_{(i,l,m)}, \hat{u}_{(i,l+1,m)}, \hat{u}_{(i,l+2,m)}, \hat{u}_{(i,l,m+1)}, \hat{u}_{(i,l,m+2)}$ are needed for $i = 1, 2, 3$, to compute these values from (3.21) and (3.22). Therefore, our form fit method, i.e., (3.16) employs many more modes compared to form fit (2.5).

Besides, our method of capturing asymptotic behavior of multidimensional Fourier coefficients, i.e., our 3D form fit (3.16), gives $C, \delta, \beta, \tilde{a}, \tilde{b}, \lambda, \mu$ which for example provides the curvature of the singular surface compared with using 1D form fit (2.5), which provides only C, δ, β.

In our numerical calculations, the Fourier transform was implemented in MATLAB 6.5. Library function $Y = \text{fft}(X)$ returns the discrete Fourier transform (DFT) of vector X, computed with a fast Fourier transform (FFT) algorithm. The same way, $Y = \text{ifft}(X)$ returns the inverse discrete Fourier transform (DFT) of vector X, computed with a fast Fourier transform (FFT) algorithm.

In the next Chapter, we validate our fitting procedure (3.16) by computing the (known) singular surface for synthetic data in two and three dimensions.

CHAPTER 4

VALIDATION OF FITTING PROCEDURE

4.1 Multidimensional Synthetic Data

In Chapter 3, we discussed the situation where $\mathbf{X}_0 = (x_0, y_0, z_0)$ is the point on the singularity surface that is closest to real (physical) space, then the singular surface near $\mathbf{X}_0$ is paraboloidal and after a rotation of variables the surface can be described as $\zeta = 0$ with

$$\zeta = x' - \mathbf{A} \cdot \mathbf{Y}' + i\mathbf{Y}' \cdot \mathbf{M}\mathbf{Y}', \tag{4.1}$$

where

$$x' = x - x_0, \quad \mathbf{Y}' = (y - y_0, z - z_0)^T. \tag{4.2}$$

In this section, for simplicity, we apply the fitting method to the synthetic data under the assumption $\mathbf{A} = \begin{pmatrix} a \\ b \end{pmatrix}$ and that $\mathbf{M}$ is a diagonal matrix given by $\mathbf{M} = \begin{pmatrix} \lambda & 0 \\ 0 & \mu \end{pmatrix}$. Hence (4.1) becomes

$$\zeta = x - x_0 - a(y - y_0) - b(z - z_0) + i[\lambda(y - y_0)^2 + \mu(z - z_0)^2]. \tag{4.3}$$

Therefore, if

$$u = u_0 \zeta^{\beta}, \tag{4.4}$$

where ζ is given by (4.3) and y_0, z_0 are real, then as shown in Chapter 3

$$\hat{u}_{\mathbf{k}} = C_\beta \exp(-i\mathbf{k} \cdot \mathbf{X}_0) k^{-(\beta+2)} \exp[\frac{-1}{4k}(k\mathbf{A} + \mathbf{l})^T \mathbf{M}^{-1}(k\mathbf{A} + \mathbf{l})], \tag{4.5}$$

or equivalently for $\mathbf{k} = (k, l, m)$

$$\ln|\hat{u}_{\mathbf{k}}| = \ln|C_\beta| - (\beta + 2)\ln k - (\delta + \frac{a^2}{4\lambda} + \frac{b^2}{4\mu})k - \frac{al}{2\lambda} - \frac{l^2}{4\lambda k} - \frac{bm}{2\mu} - \frac{m^2}{4k\mu}. \tag{4.6}$$

In this section, the fitting procedure is validated by computing the (known) singular surface for synthetic data in two dimensions.

We begin by an example of the fit for 2D synthetic data of the form

$$u = \zeta^{\beta} \quad \text{where} \quad \zeta = f(x,y) = 1 - \varepsilon_1 e^{ix} + \varepsilon_3 i \sin(y) + \varepsilon_2 \sin^2(\frac{y}{2}), \tag{4.7}$$

and $y, \varepsilon_1, \varepsilon_2, \varepsilon_3$ are real parameters while $x = x_r + ix_i$. The motivation for choosing $f(x,y)$ in the form (4.3) is that it is clearly a periodic function that (as we now show) has a singular surface in the lower half-plane of x whose local behavior near (x_0, y_0) is given by the 2D version of (4.3), i.e.,

$$\zeta = f(x,y) = x - x_0 - a(y - y_0) + i\lambda(y - y_0)^2. \tag{4.8}$$

The singular surface is given by $f(x,y) = 0$, which leads to

$$1 - \varepsilon_1 e^{i(x_r + ix_i)} + \varepsilon_3 i \sin(y) + \varepsilon_2 \sin^2(\frac{y}{2}) = 0,$$

thus

$$1 - \varepsilon_1 e^{-x_i}(\cos(x_r) + i\sin(x_r)) + \varepsilon_3 i \sin(y) + \varepsilon_2 \sin^2(\frac{y}{2}) = 0, \tag{4.9}$$

therefore,

$$1 - \varepsilon_1 e^{-x_i} \cos(x_r) + \varepsilon_2 \sin^2(\frac{y}{2}) = 0, \tag{4.10}$$

and

$$-\varepsilon_1 e^{-x_i} \sin(x_r) + \varepsilon_3 \sin(y) = 0. \tag{4.11}$$

By solving for x_i in equations (4.10) and (4.11), we obtain the two expressions

$$e^{x_i} = \frac{\varepsilon_1 \cos(x_r)}{1 + \varepsilon_2 \sin^2(\frac{y}{2})}, \tag{4.12}$$

$$e^{x_i} = \frac{\varepsilon_1 \sin(x_r)}{\varepsilon_3 \sin y}, \tag{4.13}$$

for $x = x_r + ix_i$ on the singular surface. Using (4.12) and (4.13)

$$\tan(x_r) = \frac{\varepsilon_3 \sin(y)}{1 + \varepsilon_2 \sin^2(\frac{y}{2})}, \tag{4.14}$$

hence

$$x_r = \tan^{-1}\left(\frac{\varepsilon_3 \sin(y)}{1 + \varepsilon_2 \sin^2(\frac{y}{2})}\right), \tag{4.15}$$

while (4.13) and (4.14) give,

$$x_i = \ln\left(\frac{\varepsilon_1 \cos\left(\tan^{-1}\left(\frac{\varepsilon_3 \sin(y)}{1+\varepsilon_2 \sin^2(\frac{y}{2})}\right)\right)}{1 + \varepsilon_2 \sin^2(\frac{y}{2})}\right). \tag{4.16}$$

Equations (4.15) and (4.16) give the singular curve (in $2D$)

$$x(y) = x_r(y) + ix_i(y)$$

as a function of real parameter y. Taylor expansion of (4.15) and (4.16) about $y_0 = 0$ leads to,

$$x_r = \varepsilon_3 y - (\frac{\varepsilon_3}{6} + \frac{\varepsilon_3^2}{3} + \frac{\varepsilon_3\varepsilon_2}{4})y^3 + O(y^6), \tag{4.17}$$

$$x_i = \ln(\varepsilon_1) - (\frac{\varepsilon_3^2}{2} + \frac{\varepsilon_2}{4})y^2 + O(y^3). \tag{4.18}$$

Taking $\beta = \frac{-1}{2}$ in (4.4) and comparing (4.17) and (4.18) with (4.8), lead to

$$\delta = -\ln(\varepsilon_1)\ , \quad a = \varepsilon_3, \quad \beta = -0.5, \tag{4.19}$$

$$\lambda = \frac{\varepsilon_3^2}{2} + \frac{\varepsilon_2}{4}. \tag{4.20}$$

We compare the numerical form fit with the theoretical values in (4.19) and (4.20).

4.2 2D Numerical Examples

For our first example, we use (4.7) along with the following numerical values

$$\varepsilon_1 = 0.95, \qquad \varepsilon_2 = 2, \qquad \varepsilon_3 = 0, \tag{4.21}$$

therefore, from (4.19), (4.20) and (4.21) we have

$$\beta = -0.5, \qquad \delta = -\ln(.95), \qquad a = 0, \qquad \lambda = 0.5. \tag{4.22}$$

Figure 4.1 shows a plot of the log Fourier spectrum, i.e., $\log_{10}\left|\hat{u}_{(k,l)}\right|$ versus (k,l) for the synthetic data of the form (4.7) where $\varepsilon_1, \varepsilon_2, \varepsilon_3$ are given by (4.21). Plot is for $0 \le k \le N$ and $0 \le l \le M$ where $N = M = 512$ and $\hat{u}_{(k,l)}$ for $l = [1, \frac{N}{2} + 1]$ are positive wavenumbers modes while for $l = (\frac{N}{2} + 1, N]$ are negative wavenumbers modes. We used the $2D$ version of (3.21), i.e.,

$$\begin{pmatrix} \ln\left|\hat{u}_{(k,l)}\right| \\ \ln\left|\hat{u}_{(k,l+1)}\right| \\ \ln\left|\hat{u}_{(k,l+2)}\right| \end{pmatrix} = \begin{pmatrix} 1 & l & l^2 \\ 1 & l+1 & (l+1)^2 \\ 1 & l+2 & (l+2)^2 \end{pmatrix} \begin{pmatrix} \gamma_0 \\ \gamma_1 \\ \gamma_2 \end{pmatrix} \tag{4.23}$$

By looking at the spectrum of u, i.e., the top of Figure 4.1, it seems that the slowest rate of decay of Fourier coefficients is near the edge of spectrum, i.e., near $l = 1$. Hence, in the system of equations (4.23), we fix the direction in wavenumber

space in which the matrix is inverted for $l = 1$ and increasing k. The results are similar for other l near 1. Figure 4.1 also, shows the plot of $\ln|C|$ versus k where $\ln|C|$ converges for increasing k. Figure 4.2 presents results of the sliding fit for $\beta, \delta, a, \lambda$ as a function of k, for $l = 1$ and the theoretical values for these coefficients obtained from (4.19), (4.20) (straight red lines). As Figure 4.2 indicates there is good agreement between the fits and these theoretical values. The presence of the oscillations in the fits are due to aliasing error and the fact that amplitudes of Fourier coefficients approach machine round off error; therefore, the fits degenerate.

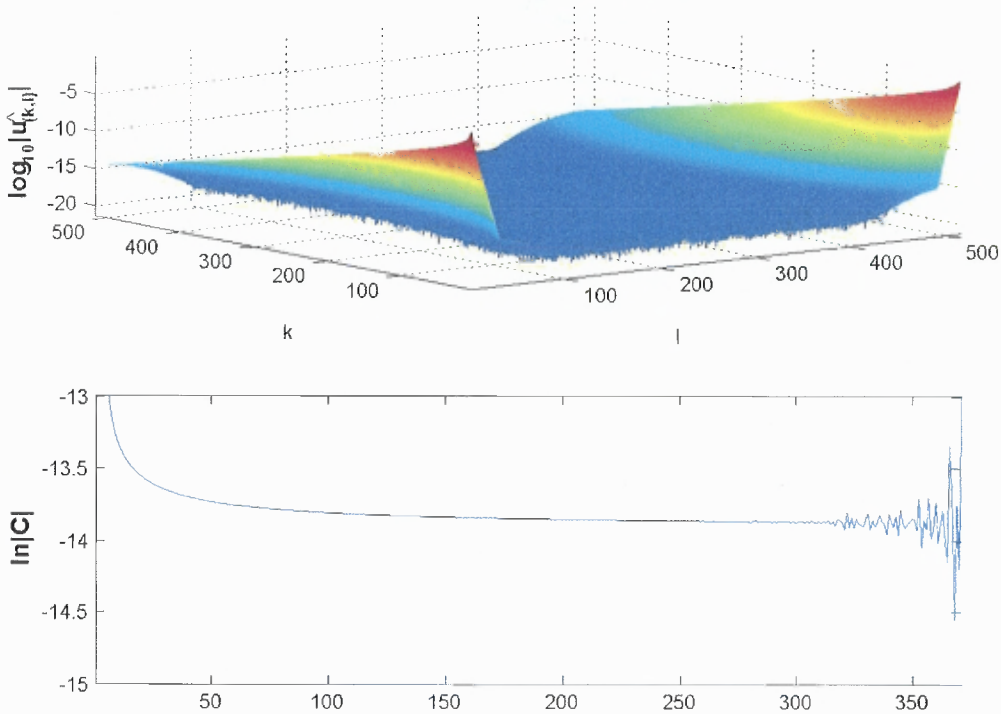

Figure 4.1 The top is plot of the Fourier transform of the linear-log scale (i.e., $\log_{10}|\hat{u}_{\mathbf{k}}|$ versus (k, l)). The bottom is the plot of sliding form fit for $\ln|C|$ versus k.

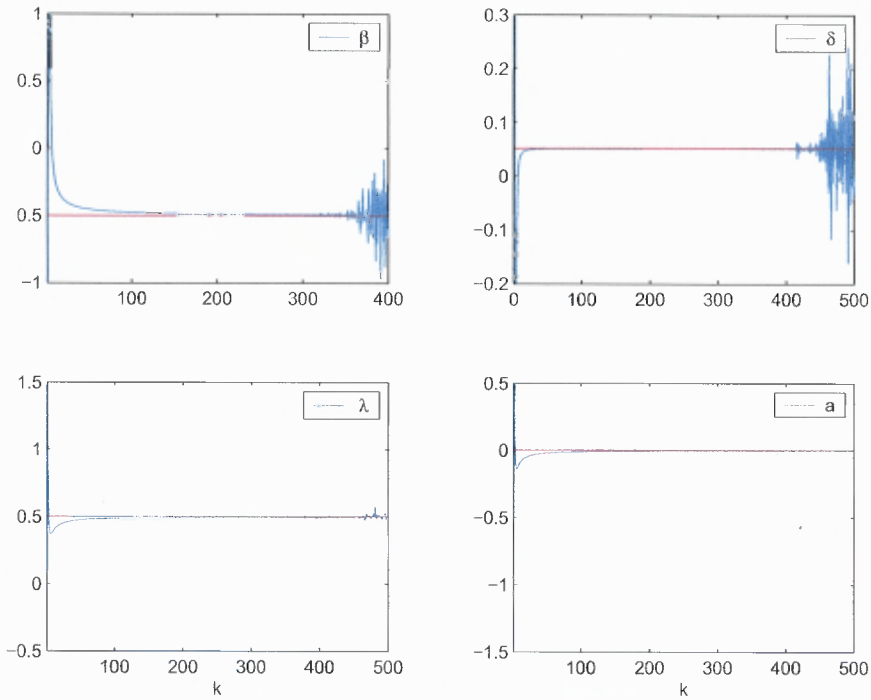

Figure 4.2 Plots of sliding form fit for β, δ, λ and a (blue curves) compared with their theoretical values (red lines).

For the next example, again consider a function $f(x, y)$ of the form (4.7), but change the value of ε_3 from 0 to -1 with other parameters the same as the previous example, i.e.,

$$\varepsilon_1 = 0.95, \qquad \varepsilon_2 = 2, \qquad \varepsilon_3 = -1, \tag{4.24}$$

then by (4.19), (4.20) and (4.24)

$$\beta = -0.5, \qquad \delta = -\ln(0.95), \qquad a = -1, \qquad \lambda = 1. \tag{4.25}$$

Figure 4.3 shows the graph of $\log_{10}\left|\hat{u}_{(k,l)}\right|$ versus (k, l) for synthetic data of the form (4.7) where $\varepsilon_1, \varepsilon_2, \varepsilon_3$ are given by (4.24). Again by careful examination of the spectrum, i.e., Figure 4.3, one obseves that the slowest rate of decay of Fourier

coefficients is near the main diagonal of matrix $\hat{u}_{(k,l)}$, i.e., $\hat{u}_{(k,k)}$. Hence, in the system of equations (4.23), we fix the direction in wavenumber space in which the matrix is inverted for $l = k$ and increasing k.

Figure 4.4 presents results of the sliding fit for $\beta, \delta, a, \lambda$ as a function of k, for $l = k$ and the theoretical values for these coefficients obtained from (4.25) (straight red lines). As Figure 4.4 indicates there is good agreement between the fits and these theoretical values. In addition, The fits are nearly equally good for parameters values near by those chosen in Figure 4.4. Again, the presence of the oscillations in the fits are due to aliasing error and the fact that amplitudes of Fourier coefficients approach machine round off error; therefore, the fits degenerate.

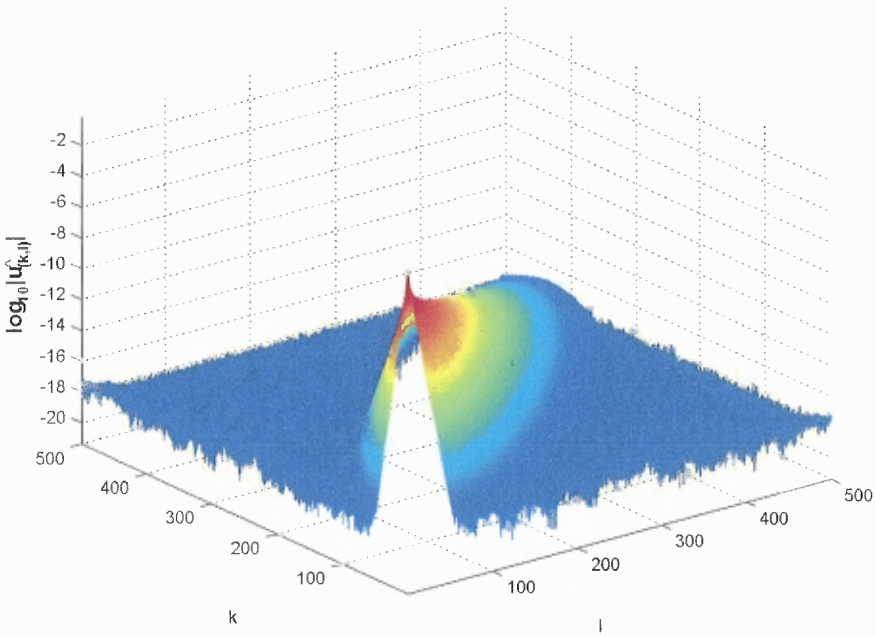

Figure 4.3 The plot is the Fourier transform of the linear-log scale (i.e., $\log_{10}|\hat{u}_{\mathbf{k}}|$ versus (k, l)).

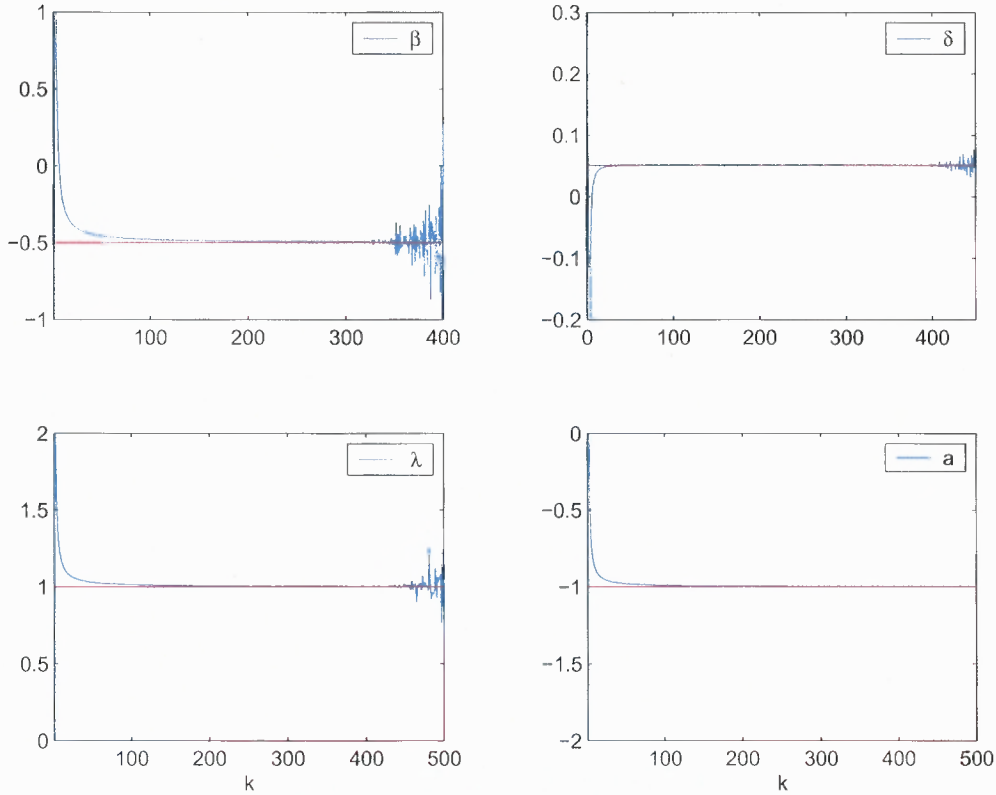

Figure 4.4 Fits for the asymptotic of the β, δ, λ and a. The fits (blue curves) are compared to theoretical values shown as red horizontal lines.

Note that for a function of the form (4.7) with a fixed values of $\varepsilon_3 = 0$ or -1 and with small changes to the values of $\varepsilon_1 = 0.95$ and $\varepsilon_2 = 2$, we would still have good agreement between the numerical values of $\beta, \delta, a, \lambda$ obtained by form fit (4.6) and their theoretical values given by relations (4.19) and (4.20).

In addition, for a function of the form (4.7) and for values of ε_3 such that $-0.3 \leq \varepsilon_3 \leq 0.3$ and $-1.3 \leq \varepsilon_3 \leq -0.7$ with $\varepsilon_1 = 0.95$ and $\varepsilon_2 = 2$, the agreements between numerical values obtained from form fit (4.6) and their theoretical values given by (4.19) and (4.20) are still acceptable.

The theory developed in sections (4.1) and (4.2) suggests that the fits to parameters $\beta(k,l), \delta(k,l)$, etc. should converge to their asymptotic values for $k \to \infty$ and l fixed. However, numerical examples show that the approach to the asymptotic limit is

nonuniform in l (this is most noticeable in Figures 4.7 and 4.8 for $\lambda(k,l)$). In practice, we find that fitting along the direction in Fourier space in which the spectrum $\left|\hat{u}_{(k,l)}\right|$ has the slowest decay gives the best fits, i.e., those that are closest to the expected (known) values. We do not have an explanation for this empirical finding. In the following, we provide examples which illustrate the nonuniform limit of $\lambda(k,l)$. We use parameter values that have been found (empirically) to be the most challenging to fit properly. Again, we consider the synthetic data (4.7) with

$$\varepsilon_1 = 0.95, \qquad \varepsilon_2 = 2, \qquad \varepsilon_3 = -0.4, \tag{4.26}$$

where by relations (4.19), (4.20) and (4.24)

$$\beta = -0.5, \qquad \delta = -\ln(.95), \qquad a = -0.5, \qquad \lambda = 0.58. \tag{4.27}$$

Figure 4.5 shows the graphs of $\log_{10}\left|\hat{u}_{(k,l)}\right|$ versus (k,l) for synthetic data of the form (4.7) where $\varepsilon_1, \varepsilon_2, \varepsilon_3$ are given by (4.26). By careful examination of Figure 4.5, it seems that the slowest decay of spectrum occurs near the edge, i.e., near $l = 1$, but not precisely along it. Figure 4.6 has been generated by fixing the direction in wavenumber space in the system of equations (4.23) in which the matrix is inverted for $l = 1$ and increasing k. The Figure shows good agreement between numerical values β and δ obtaining from form fit (4.6) and their theoretical values, i.e., (4.27). The numerical values for $\lambda(k,l)$ and $a(k,l)$ approach the expected values slowly. However, the fits hit the round off error before they reach the expected values.

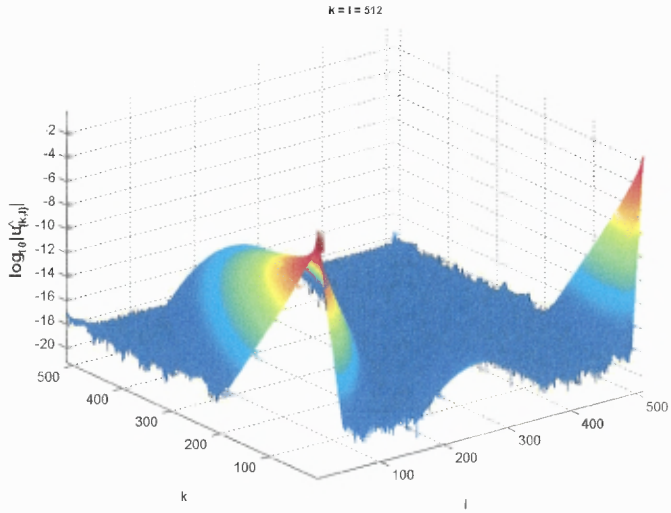

Figure 4.5 The plot is the Fourier transform of the linear-log scale (i.e., $\log_{10} |\hat{u}_{\mathbf{k}}|$ versus (k, l)).

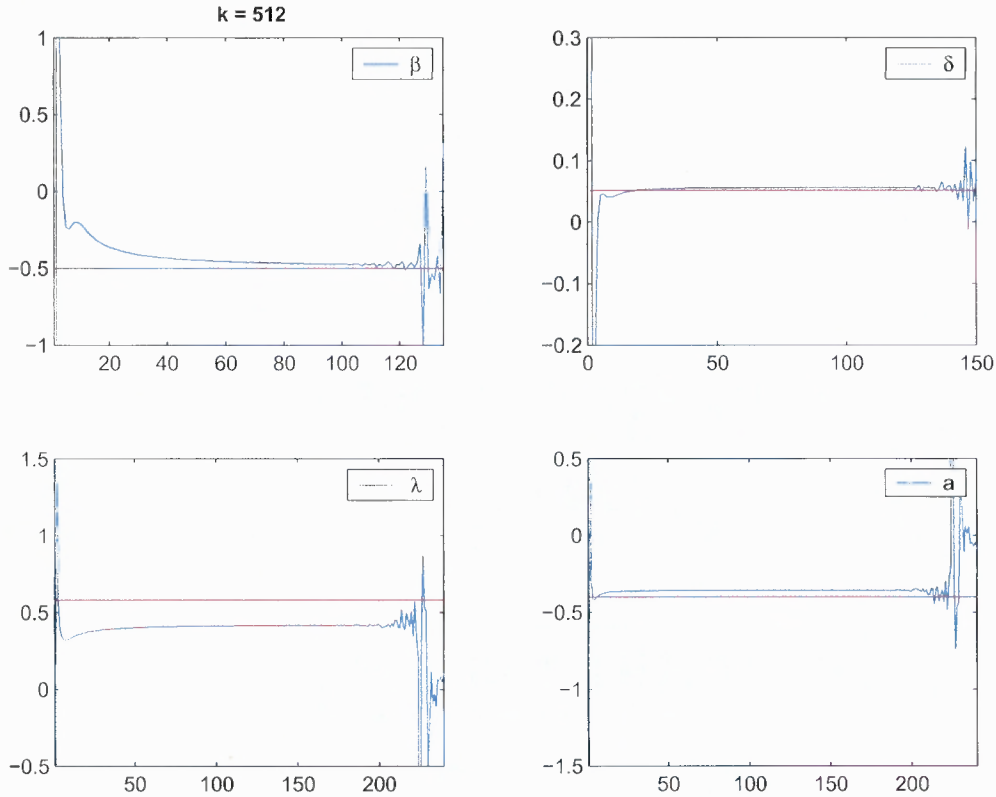

Figure 4.6 Fits for the asymptotic of the β, δ, λ and a. The fits (blue curves) are compared to theoretical values shown as a red horizontal lines.

Figure 4.7 and Figure 4.8 give a better understanding of the problem, i.e., the gap between the numerical values of $\lambda(k,l)$ and $a(k,l)$ and their theoretical values. Figure 4.7 illustrates the graph of λ, on a square block in space (k,l), more specifically $\lambda(k,l)$ versus (k,l) for $40 \leq k \leq 100$ and $1 \leq l \leq 60$. One observes that the values of $\lambda(k,l)$ for fixed l and large k approach the expected value, i.e., $\bar{\lambda} = 0.58$ along a certain direction in (k,l) space. This region in (k,l) space where the fit $\lambda(k,l)$ appears to be increasing or spreading by increasing k.

Figure 4.8 illustrates the plot of $\lambda(k,l)$ versus (k,l) for $40 \leq k \leq 235$ and $1 \leq l \leq 90$. We observe that the region in (k,l) space where the fit $\lambda(k,l)$ approaches the expected value spreads even more. The values of $\lambda(k,l)$ approach the expected value, i.e., $\bar{\lambda} = 0.58$ for a fixed l in $70 \leq l \leq 90$, and increasing k. The results are

not as good for smaller l ($l \leq 40$) and increasing k since $\lambda(k,l)$ starts to oscillate for smaller values of l and increasing k. Furthermore, it seems that as l increases, $\lambda(k,l)$ oscillate for small values of k (say $k \leq 100$). Note that in both Figures 4.7 and 4.8, taking the diagonal direction $\lambda_{(k,k)}$ along the matrix $\lambda_{(k,k)}$ would not help due to non-uniformity of $\lambda_{(k,l)}$.

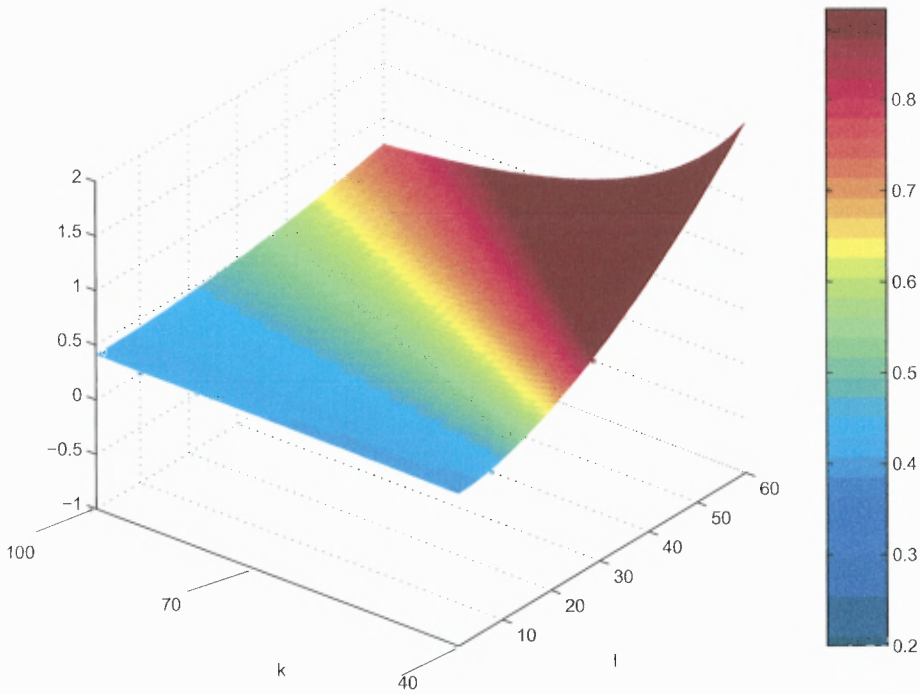

Figure 4.7 The plot of λ versus (k,l) for the range $40 \leq k \leq 100$, $1 \leq l \leq 60$.

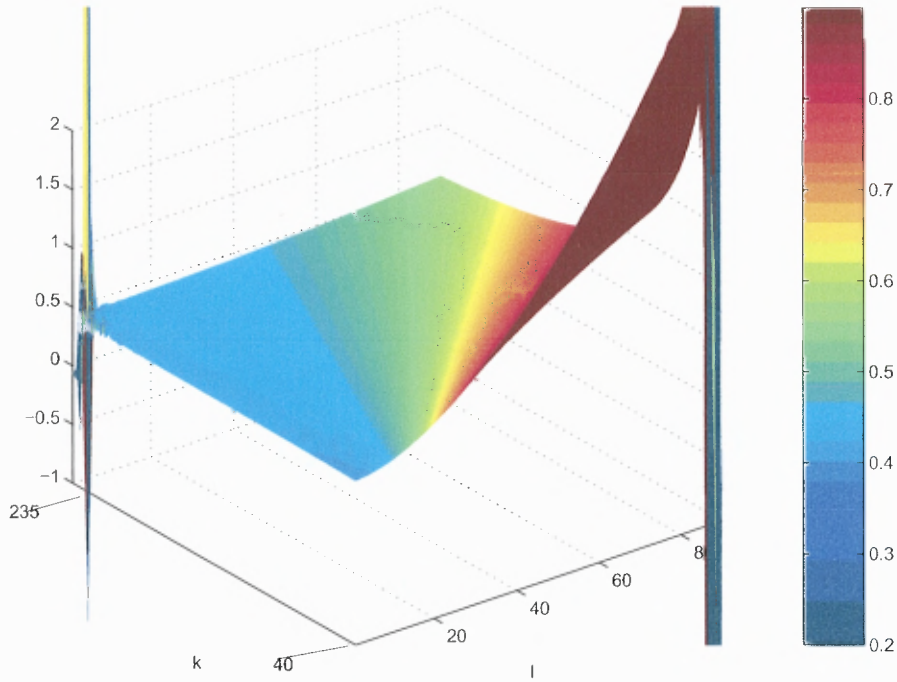

Figure 4.8 The plot of λ versus (k, l) for the range $40 \leq k \leq 235$, $1 \leq l \leq 90$.

Above discussion suggests that in the system of equations (4.23), we fix the direction in wavenumber space in which the matrix is inverted for $l = 90$ and increasing k. The results are similar for other l near 90. Figure 4.9 illustrate $a(k, l)$ and $\lambda(k, l)$ for $l = 90, 110, 130$. As we expect, there is good agreement between numerical values obtained by from form fit (4.6) and their theoretical values given by (4.27).

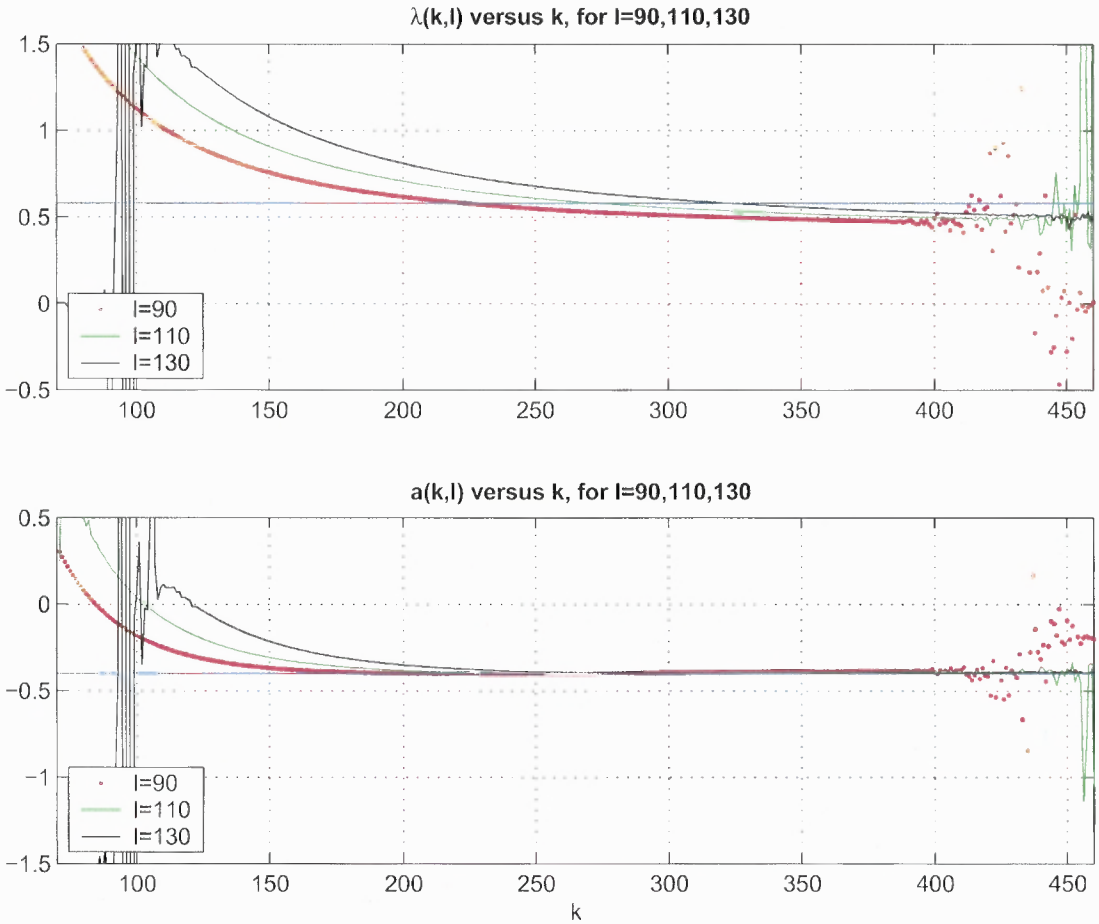

Figure 4.9 The top is the plots of $\lambda(k,l)$ versus k for $l = 90, 110, 130$. The bottom is the plots of a(k,l) versus k for $l = 90, 110, 130$. The fits (curves) are compared to theoretical values shown as horizontal lines.

4.3 3D Numerical Example

In this section, we validate our fitting procedure (3.16) by computing the (known) singular surface for synthetic data in three dimensions. Here we present an example of the fit for synthetic data of the form

$$u = \zeta^{\beta}$$

where

$$\zeta = f(x,y,z) = 1 - \varepsilon_1 \exp(ix) + \varepsilon_2 i \sin(y) + \varepsilon_3 i \sin(z) + \varepsilon_4 \sin^2(\frac{y}{2}) + \varepsilon_5 \sin^2(\frac{z}{2}), \quad (4.28)$$

and $y, z, \varepsilon_1, \varepsilon_2, \varepsilon_3, \varepsilon_4, \varepsilon_5$ are real parameters while $x = x_r + ix_i$. The motivation for choosing $f(x,y,z)$ in the form (4.3) is that it is clearly a periodic function that (as we now show) has a singular surface in the lower half-plane of x whose local behavior near $\mathbf{X}_0$ is given by (4.3). The singular parabolic surface is given by $f(x,y,z) = 0$. Following the $2D$ example (4.7),

$$x_r = \tan^{-1}\left(\frac{\varepsilon_2 \sin y + \varepsilon_3 \sin z}{1 + \varepsilon_4 \sin^2(\frac{y}{2}) + \varepsilon_5 \sin^2(\frac{z}{2})}\right), \quad (4.29)$$

and

$$x_i = \ln(\varepsilon_1) + \ln\left(\frac{\cos\left(\tan^{-1}\left(\frac{\varepsilon_2 \sin y + \varepsilon_3 \sin z}{1+\varepsilon_4 \sin^2(\frac{y}{2}) + \varepsilon_5 \sin^2(\frac{z}{2})}\right)\right)}{1 + \varepsilon_4 \sin^2(\frac{y}{2}) + \varepsilon_5 \sin^2(\frac{z}{2})}\right). \quad (4.30)$$

Equations (4.29) and (4.30) give the singular surface (in $3D$)

$$x(y,z) = x_r(y,z) + ix_i(y,z),$$

as a function of real parameter y and z. Taylor expansion of (4.29) and (4.30) about $(y_0, z_0) = (0,0)$ leads to

$$x_r = \varepsilon_2 y + \varepsilon_3 z + \text{higher order terms}, \quad (4.31)$$

$$x_i = \ln \varepsilon_1 - (\frac{\varepsilon_4}{4} + \frac{\varepsilon_2^2}{2})y^2 - (\frac{\varepsilon_5}{4} + \frac{\varepsilon_3^2}{2})z^2 - (\varepsilon_2\varepsilon_3)yz + \text{higher order terms}. \quad (4.32)$$

Taking $\beta = \frac{-1}{2}$ in (4.28), $\varepsilon_3 = 0$ in (4.32) and comparing expansions (4.31) and (4.32) with expression (4.3), lead to

$$\delta = -\ln(\varepsilon_1), \quad \beta = -\frac{1}{2}, \quad \lambda = \frac{\varepsilon_4}{4} + \frac{\varepsilon_2^2}{2}, \quad \mu = \frac{\varepsilon_5}{4} + \frac{\varepsilon_3^2}{2}, \quad a = \varepsilon_2, \quad b = \varepsilon_3. \tag{4.33}$$

To have a smooth spectrum with slow decay we have chosen the following numerical values for $\varepsilon_1, \varepsilon_2, \varepsilon_3, \varepsilon_4$ and ε_5

$$\varepsilon_1 = 0.985, \qquad \varepsilon_2 = -0.975, \qquad \varepsilon_3 = 0, \qquad \varepsilon_4 = \varepsilon_5 = 4,$$

hence

$$\beta = -\frac{1}{2}, \quad \delta = -\ln(0.985), \quad a = -0.975, \quad b = 0, \quad \lambda = 1.475, \quad \mu = 1. \tag{4.34}$$

Figure 4.10 shows results for the sliding fit for $\beta, \delta, \lambda, \mu, a, b$ as a function of k, using form fit (4.6) and their theoretical values given by (4.34).

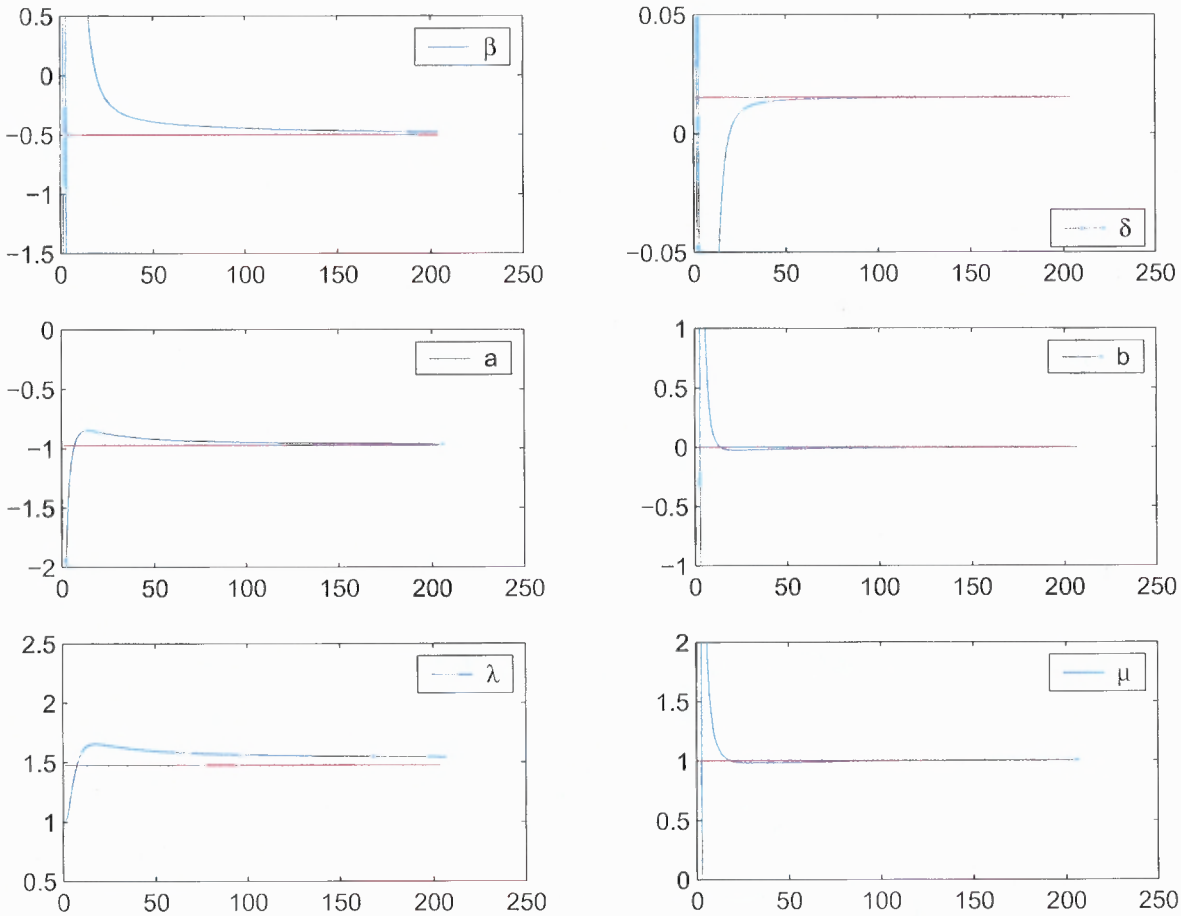

Figure 4.10 Fits for the asymptotic of the Fourier coefficients $\hat{u}_{(k,l,m)}$ in the 3D transform. The fits (blue curves) are compared to theoretical values, shown as red horizontal lines.

CHAPTER 5

TRACING COMPLEX SINGULARITIES OF BURGER'S EQUATION

5.1 The 2D Inviscid Burger's Equation

In Cartesian coordinate $\mathbf{X} = (x, y)$ the 2D inviscid Burger's equation is given by

$$\frac{\partial \mathbf{u}}{\partial t} + \mathbf{u} \cdot \nabla \mathbf{u} = \mathbf{0}, \qquad \mathbf{u}|_{t=0} = \mathbf{u}_0, \tag{5.1}$$

where $\mathbf{u} = (u, v)$ is the velocity field. Equation (5.1) is here supplemented by boundary conditions which are periodic in x, y. In this Chapter, every time we mention Burger's equation, we mean (5.1). As an example of our fitting procedure, we employ the fit (4.6) to numerical solutions of (5.1) in Fourier space to trace singular solutions (curves) of Burger's equation. We start in subsection 5.1.1 by considering complex solutions to equation (5.1). The complex Burger's equation take the same form as Burger's equation (5.1) but allow velocity $\mathbf{u} = (u, v)$ to be complex. Following Caflisch and Siegel [11], [40] we look for complex solutions which have the form of traveling waves with imaginary wave speed. The motivation for considering these solutions is that they can be computed very accurately without truncation and aliasing error. This leads to very clean fits, and is therefore useful for illustrating the method. In section 5.2, we solve the real-valued Burger's equation by a pseudospectral method, and perform the fits to ascertain the location and nature of the singular curve, as an illustration of the method.

5.1.1 Complex Traveling Wave Solutions

The investigation of complex space singularities for PDEs, which are suspected of having singular solutions, is partly motivated by the fact that real singularities (if they exist) are preceded by the formation of complex-space singularities, which move

onto the real-space domain. Besides, a study of complex singular solution of a PDE (say Euler equations) may give useful information concerning the generic singularity type of the real PDE. Li and Sinai [24] investigated complex singular solutions to the 3D Navier Stokes equations. Pauls et al. [35] numerically investigated complex space singularities to the 2D Euler equations in the short time asymptotic regime, when the singularities are far from the real domain. Caflisch [9] and Caflisch and Siegel [11] constructed complex singular solution to the Euler equations for axisymmetric flow with swirl. In the following, we discuss our method of computing solutions to the complex Burger's equation in the form of traveling waves.

We write (5.1) with a forcing term (the reason for forcing will become apparent later) in x and y components,

$$\frac{\partial u}{\partial t} + u\frac{\partial u}{\partial x} + v\frac{\partial u}{\partial y} = f^{(x)}, \tag{5.2}$$

$$\frac{\partial v}{\partial t} + u\frac{\partial v}{\partial x} + v\frac{\partial v}{\partial y} = f^{(y)}, \tag{5.3}$$

look for an upper analytic complex traveling wave solution $\mathbf{u} = (u, v)$

$$u = \sum_{\mathbf{k}>\mathbf{0}} \hat{u}_{\mathbf{k}} \exp[(\sigma.\mathbf{k})t + i(\mathbf{k}.\mathbf{x})], \tag{5.4}$$

$$v = \sum_{\mathbf{k}>\mathbf{0}} \hat{v}_{\mathbf{k}} \exp[(\sigma.\mathbf{k})t + i(\mathbf{k}.\mathbf{x})], \tag{5.5}$$

where $\mathbf{x} = (x, y), \mathbf{k} = (k, l), \sigma = (\sigma_x, \sigma_y)$, and the notation $\mathbf{a} < \mathbf{b}$ for vector quantities $\mathbf{a}$ and $\mathbf{b}$ signifies the inequality holds for at least one component, with the other components satisfying $a_i \leq b_i$. Therefore, $\mathbf{k} > \mathbf{0}$ means $k \geq 0, l \geq 0$, but $k + l \geq 1$.

Note that we discuss the motivation of choosing only positive modes in (5.4) and (5.5) later on in this section. Also,

$$f^{(x)} = \sum_{\mathbf{k}>\mathbf{0}} \hat{f}_{\mathbf{k}}^{(x)} \exp[(\sigma.\mathbf{k})t + i(\mathbf{k}.\mathbf{x})], \tag{5.6}$$

$$f^{(y)} = \sum_{\mathbf{k}>\mathbf{0}} \hat{f}_{\mathbf{k}}^{(y)} \exp[(\sigma.\mathbf{k})t + i(\mathbf{k}.\mathbf{x})]. \tag{5.7}$$

We are most interested in the case when σ_x, and σ_y are real which corresponds to a traveling wave with an imaginary wave speed. The forcing (5.6) and (5.7) are employed to generate instability in the solution. We restrict the forcing (5.6) and (5.7) to a finite number of nonzero waves modes, so the forcing is analytic. In our proposed computation, data is given by specifying the lowest wavenumber modes given below,

$$\hat{u}_{(1,0)}, \hat{v}_{(1,0),}, \hat{u}_{(0,1)}, \hat{v}_{(0,1)},$$

the next step is to find

$$\hat{u}_{(1,1)}, \hat{v}_{(1,1)},$$

in terms of lower wavenumber modes. In general, we find the $\mathbf{k}$ wavenumber modes of $\hat{\mathbf{u}}_{\mathbf{k}}$ in terms of smaller $\mathbf{k}'$ wavenumber modes of $\hat{\mathbf{u}}_{\mathbf{k}'}$ where $\mathbf{k}' < \mathbf{k}$. It is convenient to denote the nonlinear parts of equations (5.2) and (5.3), respectively by $N^{(x)}$ and $N^{(y)}$ that is,

$$N^{(x)} = u\frac{\partial u}{\partial x} + v\frac{\partial u}{\partial y}, \tag{5.8}$$

$$N^{(y)} = u\frac{\partial v}{\partial x} + v\frac{\partial v}{\partial y}, \tag{5.9}$$

where

$$N^{(x)} = \sum_{\mathbf{k}>0} \hat{N}_{\mathbf{k}}^{(x)} \exp[(\sigma.\mathbf{k})t + i(\mathbf{k}.\mathbf{x})], \tag{5.10}$$

$$N^{(y)} = \sum_{\mathbf{k}>0} \hat{N}_{\mathbf{k}}^{(y)} \exp[(\sigma.\mathbf{k})t + i(\mathbf{k}.\mathbf{x})]. \tag{5.11}$$

We calculate Fourier modes by substituting (5.4) - (5.7) into (5.1) and after some algebraic manipulation

$$(\sigma.\mathbf{k})\hat{u}_{\mathbf{k}} = -\hat{N}_{\mathbf{k}}^{(x)} + \hat{f}_{\mathbf{k}}^{(x)}, \tag{5.12}$$

$$(\sigma.\mathbf{k})\hat{v}_{\mathbf{k}} = -\hat{N}_{\mathbf{k}}^{(y)} + \hat{f}_{\mathbf{k}}^{(y)}. \tag{5.13}$$

In our solution method, we choose the (unstable) traveling wave speed and a set of low wavenumber unstable modes, and then solve for the forcing and higher wavenumber modes generated by nonlinearity. For simplicity, let us assume

$$\sigma = (\sigma_x, \sigma_y) = (1, 1),$$

therefore, relations (5.12) and (5.13) become

$$(k + l)\hat{u}_{\mathbf{k}} = -\hat{N}_{\mathbf{k}}^{(x)} + \hat{f}_{\mathbf{k}}^{(x)}, \tag{5.14}$$

$$(k + l)\hat{v}_{\mathbf{k}} = -\hat{N}_{\mathbf{k}}^{(y)} + \hat{f}_{\mathbf{k}}^{(y)}. \tag{5.15}$$

The following modes are given as data:

$$\hat{u}_{(1,0)}, \hat{u}_{(0,1)}, \hat{v}_{(1,0)}, \hat{v}_{(0,1)}, \tag{5.16}$$

to start suppose

$$\mathbf{k} = (1,0) \text{ that is } k = 1, l = 0,$$

then by using (5.14) and (5.15),

$$\begin{aligned} \hat{f}^{(x)}_{(1,0)} &= \hat{u}_{(1,0)}, \\ \hat{f}^{(y)}_{(1,0)} &= \hat{v}_{(1,0)}, \end{aligned}$$

where we have used

$$\begin{aligned} \hat{N}^{(x)}_{(1,0)} &= 0, \\ \hat{N}^{(y)}_{(1,0)} &= 0. \end{aligned}$$

In the same way, we find

$$\begin{aligned} \hat{f}^{(x)}_{(0,1)} &= \hat{u}_{(0,1)}, \\ \hat{f}^{(y)}_{(0,1)} &= \hat{v}_{(0,1)}. \end{aligned}$$

Note that the forcing modes are chosen so that the equation for $\hat{\mathbf{u}}_{\mathbf{k}}$ is exactly satisfied when $|\mathbf{k}| = 1$ where

$$|\mathbf{k}| = k + l.$$

We turn off the body forces for the modes higher than 1 now that we have calculated quantities (5.16). In other words,

$$\hat{f}^{(x)}_{\mathbf{k}} = \hat{f}^{(y)}_{\mathbf{k}} = 0 \quad \text{for} \quad \mathbf{k} = (k,l) \quad \text{where} \quad |\mathbf{k}| \geq 2.$$

Therefore, expresions (5.14) and (5.15) become,

$$\hat{u}_{(k,l)} = \frac{-\hat{N}^{(x)}_{(k,l)}}{k+l}, \tag{5.17}$$

$$\hat{v}_{(k,l)} = \frac{-\hat{N}^{(y)}_{(k,l)}}{k+l}. \tag{5.18}$$

Since each of the nonlinear terms $\hat{N}^{(x)}_{(k,l)}$, $\hat{N}^{(y)}_{(k,l)}$ only depend on modes of $\hat{u}_{(k',l')}$ and $\hat{v}_{(k',l')}$ where

$$2 \leq k' + l' < k + l,$$

the system of equations (5.17) and (5.18) are solvable. Before presenting numerical results, we provide an example of calculation of the velocity Fourier coefficients for $\mathbf{k} = (1,1)$, i.e, $\hat{u}_{(1,1)}$ and $\hat{v}_{(1,1)}$. Suppose

$$\hat{u}_{(1,0)}, \hat{u}_{(0,1)}, \hat{v}_{(1,0)}, \hat{v}_{(0,1)},$$

are given. By using (5.10) and (5.11), let us calculate the values of

$$\hat{u}_{(1,1)}, \hat{v}_{(1,1)}.$$

First, by relations (5.8) and (5.9),

$$N^{(x)}_{(1,1)} = i\hat{u}_{(0,1)}(\hat{u}_{(1,0)} + \hat{v}_{(1,0)}) \exp[2t + i(x+y)],$$

$$N^{(y)}_{(1,1)} = i\hat{v}_{(1,0)}(\hat{u}_{(0,1)} + \hat{v}_{(0,1)}) \exp[2t + i(x+y)].$$

Therefore, relations (5.10) and (5.11) give

$$\hat{N}^{(x)}_{(1,1)} = i\hat{u}_{(0,1)}(\hat{u}_{(1,0)} + \hat{v}_{(1,0)}), \tag{5.19}$$

$$\hat{N}^{(y)}_{(1,1)} = i\hat{v}_{(1,0)}(\hat{u}_{(0,1)} + \hat{v}_{(0,1)}). \tag{5.20}$$

Starting with

$$\hat{u}_{(1,0)} = \hat{u}_{(0,1)} = \epsilon_1 = 0.2375, \text{ and } \hat{v}_{(1,0)} = \hat{v}_{(0,1)} = 0.262, \tag{5.21}$$

and substituting (5.21) in (5.19) and (5.20), one obtains

$$\hat{N}^{(x)}_{(1,1)} = 0.1186i, \text{ and } \hat{N}^{(y)}_{(1,1)} = 0.1309i.$$

Hence, from relations (5.17) and (5.18)

$$\hat{u}_{(1,1)} = -\frac{0.1186i}{2}, \text{ and } \hat{v}_{(1,1)} = -\frac{0.1309i}{2}.$$

The same way, one can generate other wavenumber modes, i.e., $\hat{u}_{(1,2)}, \hat{u}_{(2,1)}, \hat{v}_{(1,2)}, \hat{v}_{(2,1)}$, etc., which we do numerically.

In other usually more complicated problems (i.e., 3D problems) advantages have been gained by restricting attention to periodic solutions with only non-negative wavenumbers $\mathbf{k} > \mathbf{0}$ and to traveling wave solutions:

(i) The dimensionality of the problem is reduced, by eliminating the time variable.

(ii) Because the sums (5.4) and (5.5) involve only positive wavenumbers, i.e.,

$$\begin{pmatrix} \hat{u}_{(k,l)} \\ \hat{v}_{(k,l)} \end{pmatrix} = \begin{pmatrix} \frac{-1}{k+l} & 0 \\ 0 & \frac{-1}{k+l} \end{pmatrix} \begin{pmatrix} \hat{N}^{(x)}_{(k,l)} \\ \hat{N}^{(y)}_{(k,l)} \end{pmatrix}. \tag{5.22}$$

where $\hat{N}^{(x)}_{(k,l)}$, $\hat{N}^{(y)}_{(k,l)}$ only depend on $\hat{u}_{(k',l')}$ and $\hat{v}_{(k',l')}$ and $k' + l' < k + l$, there is only a one-way coupling between wavenumbers. That $\mathbf{k}$ is only influenced by $\mathbf{k}'$ with $\mathbf{k}' < \mathbf{k}$.

The one way coupling between wavenumbers also means that there is no truncation error introduced by the restriction to finite $\mathbf{k}$. The nonlinear terms $\hat{N}^{(x)}_{(k,l)}$ and $\hat{N}^{(y)}_{(k,l)}$ in the system of equations (5.22) is computed using a pseudospectral method, and there are only quadratic nonlinearities, aliasing error can be completely eliminated by padding with zeros.

Figure 5.1 shows the graph of $\log_{10}\left|\hat{u}_{(k,l)}\right|$ versus (k,l) for initial data of the form (5.21). By careful examination of the spectrum of u, i.e., Figure 5.1, we can observe that the slowest rate of decay of Fourier coefficients is near the main diagonal of matrix $\hat{u}_{(k,l)}$, i.e. $\hat{u}_{(k,k)}$. Therefore, in the system of equations (4.23), we fix the direction in wavenumber space in which the matrix is inverted for $l = k$ and increasing k. The plot of $\log_{10}\left|\hat{v}_{(k,l)}\right|$ is almost the same hence, we do not present it here.

Figure 5.2 presents results of the sliding fit for $\beta, \delta, a, \lambda$ as a function of k, for $l = k$. The results obtained for initial data of (5.21) and the plot is for $0 \leq k \leq N$ and $0 \leq l \leq M$ where $N = M = 128$ for the triangles and $N = M = 256$ for the blue curves. Numerical results of the sliding fit for $\beta, \delta, a, \lambda$ for v is almost the same and has not been presented here. The fits shown in the figure are very clean. In particular, the fit to the singular exponent gives the expected square root singularity, which is the generic complex singularity for Burger's equation.

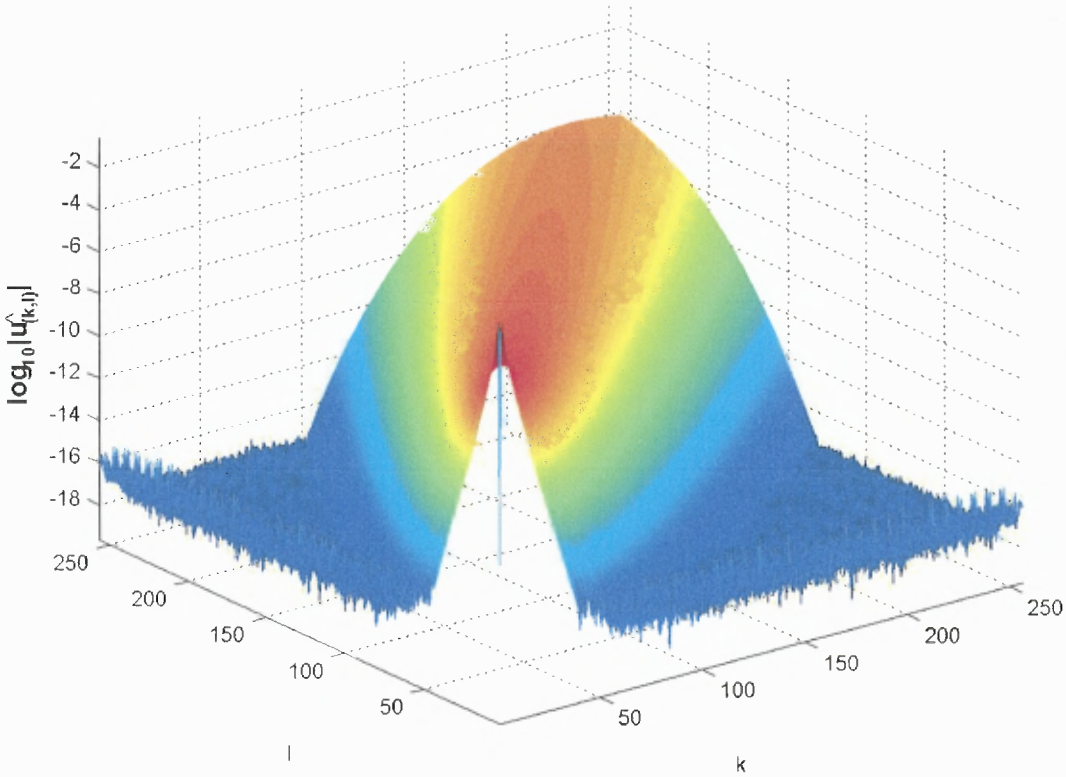

Figure 5.1 The plot is the Fourier transform of the linear-log scale (i.e., $\log_{10}|\hat{u}_{(k,l)}|$ versus (k,l)). The plot is for $0 \leq k \leq N$ and $0 \leq l \leq M$ where $N = M = 256$.

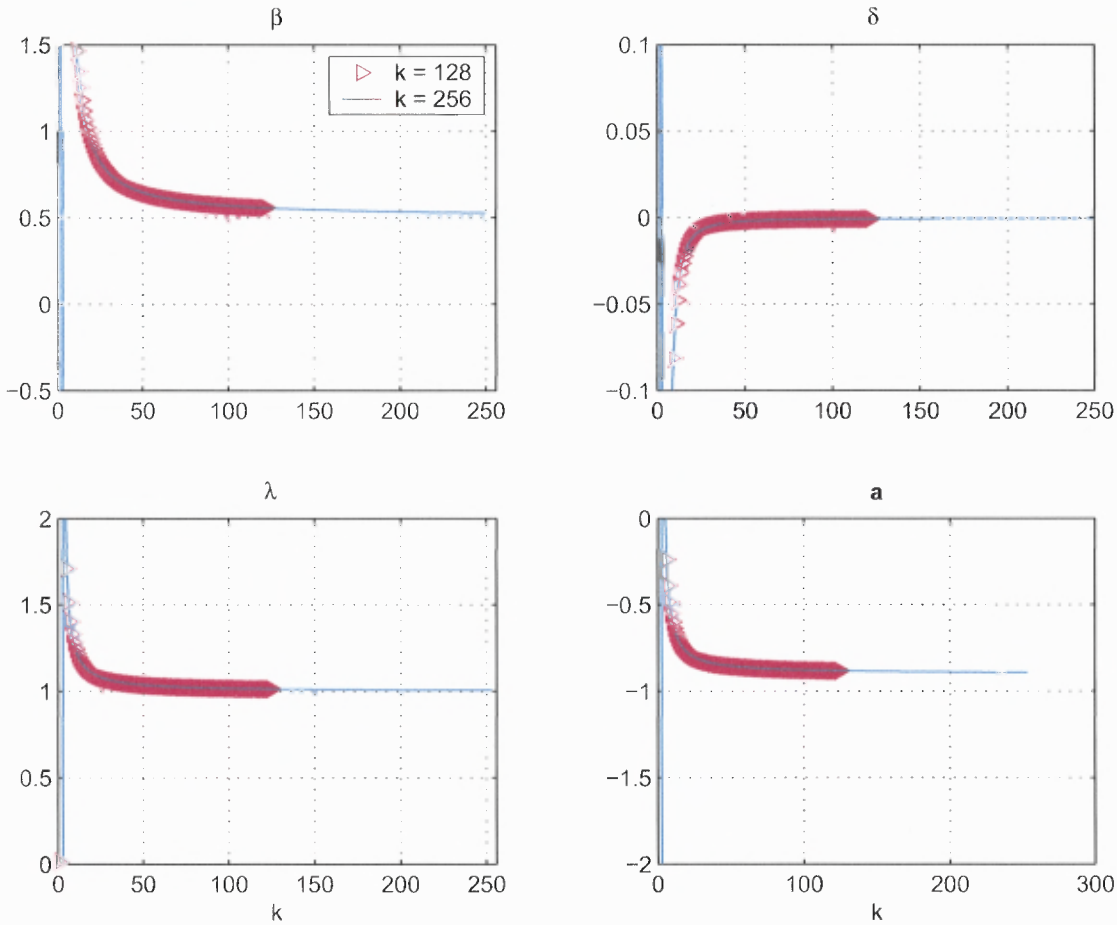

Figure 5.2 Fits for the asymptotic of the β, δ, λ and a for the Burger's equation. The fits for $k = l = 128$ (triangles) compared to the fits for $k = l = 256$ (blue curves).

5.1.2 More Numerical Examples

From sums (5.4) and (5.5)

$$u = \sum_{\mathbf{k}>0} \hat{u}_{\mathbf{k}} \exp i\mathbf{k}\cdot(\mathbf{x}-i\sigma t), \tag{5.23}$$

$$v = \sum_{\mathbf{k}>\mathbf{0}} \hat{v}_{\mathbf{k}} \exp i\mathbf{k}\cdot(\mathbf{x}-i\sigma t), \tag{5.24}$$

Consider $\sigma = (1, i)$ in (5.23) and (5.24) then

$$u = \sum_{k>0,l>0} \hat{u}_{(k,l)} e^{ik(x-it)} e^{il(y+t)},$$

$$v = \sum_{k>0,l>0} \hat{v}_{(k,l)} e^{ik(x-it)} e^{il(y+t)}.$$

Therefore, $\mathbf{u}(x - it, y + t)$ is a growing wave solution which translates with a constant real speed in $(0, -1)$ direction. A singularity with imaginary component

$$\delta = -Im\ x$$

at $t = 0$ will hit the real x line at $t = \delta$. The singularity positions also depend on y, i.e., $\delta = \delta(y)$ and the first singularity occurs for y, that minimize δ. Thus a singularity will occur at a real space point if the computed traveling wave solutions (5.23) or (5.24) has a singularity at any complex value of x. Note that one could have employed $\sigma = (1, 0)$ in (5.23) and (5.24). However, we choose $\sigma = (1, i)$ in calculation of finding higher wavenumber modes to avoid 0 divisor problem.

We use the following modes as given data to generate traveling waves solutions correspond to $\sigma = (1, i)$

$$\hat{u}_{(1,0)} = \hat{u}_{(0,1)} = \frac{\epsilon_1}{\sigma_x}, \quad \hat{v}_{(1,0)} = \hat{v}_{(0,1)} = \frac{\epsilon_2}{\sigma_y}, \tag{5.25}$$

where

$$\epsilon_1 = 0.2, \quad \epsilon_2 = 0.22, \quad \text{and} \quad \sigma_x = 1, \quad \sigma_y = i. \tag{5.26}$$

By following the exact same procedure as our first example, we generate higher wavenumber modes.

Figure 5.3 illustrates the plot of $\log_{10}\left|\hat{u}_{(k,l)}\right|$ versus (k,l) for initial data (5.25) and (5.26). By careful examination of the spectrum of u, i.e., Figure 5.3, one observes that the slowest rate of decay of Fourier coefficients is near the main diagonal of matrix $\hat{u}_{(k,l)}$, i.e., $\hat{u}_{(k,k)}$. Therefore, in the system of equations (4.23), we fix the direction in wavenumber space in which the matrix is inverted for $l = k$ and increasing k. The plot of $\log_{10}\left|\hat{v}_{(k,l)}\right|$ is almost the same hence, we do not present it here.

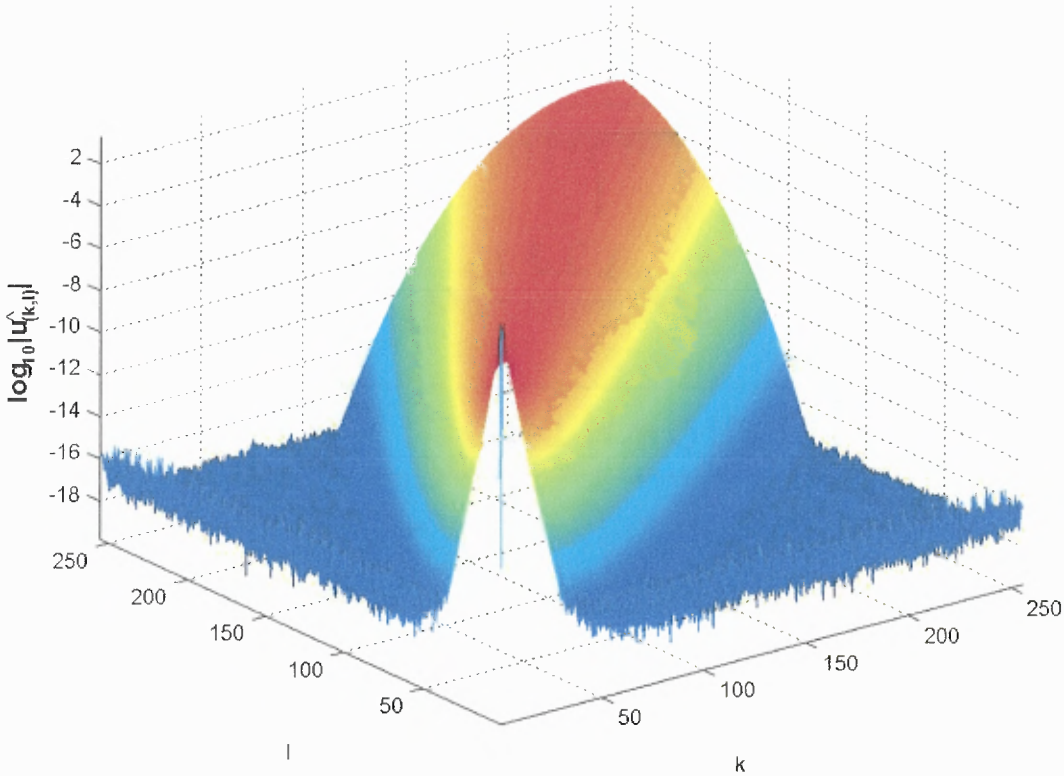

Figure 5.3 The plot is the Fourier transform of the linear-log scale (i.e., $\log_{10}|\hat{u}_{(k,l)}|$ versus (k,l)). The plot is for $0 \leq k \leq N$ and $0 \leq l \leq M$ where $N = M = 256$.

Figure 5.4 presents results of the sliding fit for $\beta, \delta, a, \lambda$ as a function of k, for $l = k$. The results obtained for initial data (5.25) and (5.26) where the plot is for $0 \leq k \leq N$ and $0 \leq l \leq M$ where $N = M = 128$ for the triangles and $N = M = 256$ for the blue curves. Numerical results of the sliding fit for $\beta, \delta, a, \lambda$ for v is almost the same and has not been presented here.

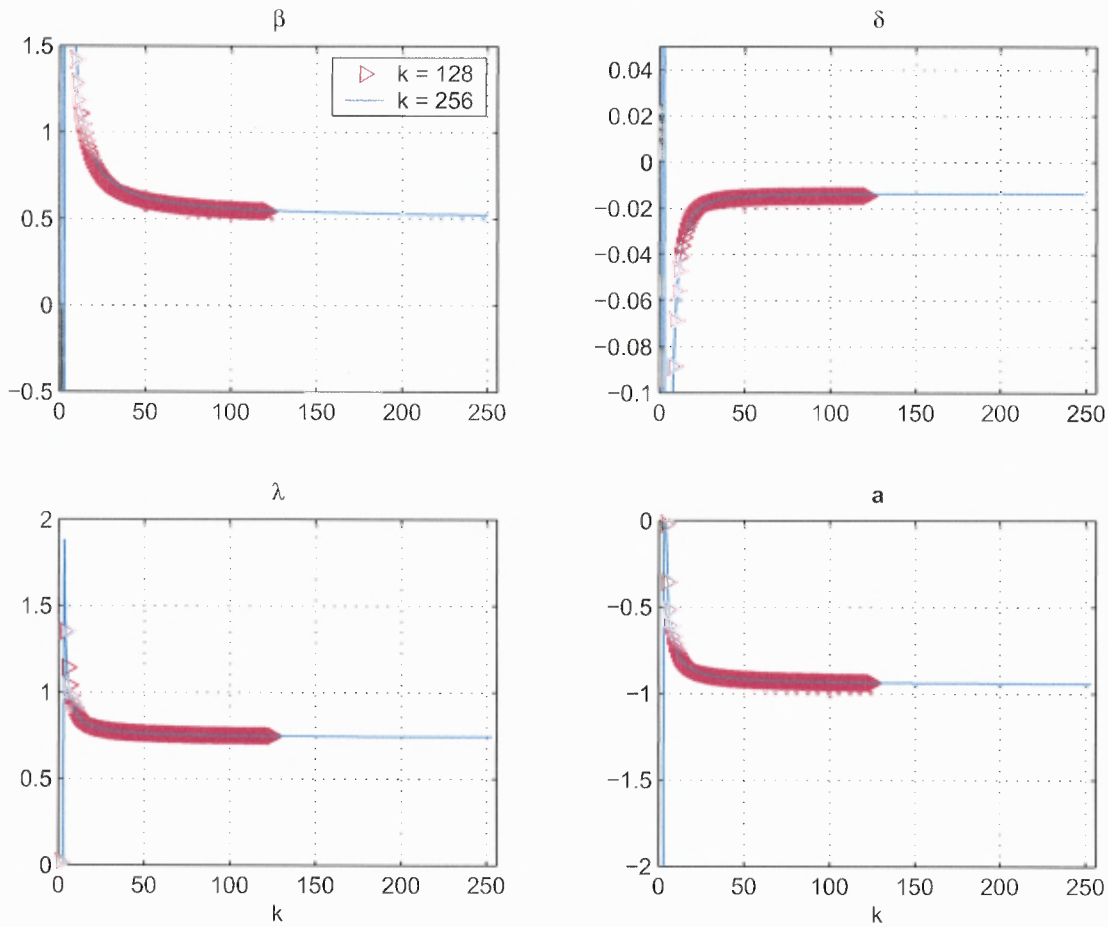

Figure 5.4 Fits for the asymptotic of the β, δ, λ and a for the Burger's Equations. The fits for $k = l = 128$ (triangles) compared to the fits for $k = l = 256$ (blue curves).

In the next section, instead of using traveling wave solution, we take a different approach and employ pseudospectral method to solve a version of Burger's equation (5.1) directly. Then we employ our multidimensional form fit to obtain $\beta, \delta, a, \lambda$ for our numerical solution.

5.2 Singularity Fits for the Initial Value Problem of 2D Burger's Equation

In Cartesian coordinate $\mathbf{x} = (x, y)$, a simplified version of 2D inviscid Burger's equation is given by

$$\frac{\partial u}{\partial t} + uu_x + uu_y = 0, \quad u|_{t=0} = u_0, \tag{5.27}$$

where $u = u(x, y)$ is the velocity field. Equation (5.27) is supplemented by boundary condition which depend on the particular problem. We assume the velocity field to be periodic in x, y. Note that the equation (5.27) can be transformed to 1D Burger's equation with the change of variable $z = x+y$. Hence, one can find the implicit exact solution of (5.27). However, there is a parametric dependence on second dimension for the initial condition presented here (see (5.28)). Therefore, (5.27) plus the initial condition is a 2D initial value problem.

Consider equation (5.27) with the following initial condition,

$$u_0 = u(x, y, 0) = \varepsilon \cos(x - y) - \sin(x) - \cos(y), \tag{5.28}$$

where $\varepsilon = -0.05$.

To find the numerical solution of (5.27) with the initial condition (5.28), we apply pseudospectral method. In this approach, we use leap frog formula for the time derivatives and approximate the spatial derivatives spectrally, precisely, we use FFT to approximate spatial derivatives. The leap-frog scheme requires two initial conditions to start with, whereas the PDE (5.27) provides only one. To obtain another starting value, second order Runge-Kutta formula has been employed. Numerical results are given in Figure 5.5 and 5.6.

Figure 5.5 presents numerical solution of (5.27) with the initial condition (5.28), i.e., u at $t = 0.45$ (the top plot) and its spectrum (the bottom plot). By careful examination of the spectrum of u, i.e., Figure 5.5, one observes that the slowest rate of decay of Fourier coefficients is along the main diagonal of matrix $\hat{u}_{(k,l)}$, i.e., $\hat{u}_{(k,k)}$. Therefore, in the system of equations (4.23), we fix the direction in wavenumber space

in which the matrix is inverted for $l = k$ and increasing k. The plot is for $0 \leq k \leq N$ and $0 \leq l \leq M$ where $N = M = 256$.

Figure 5.6 presents results of the sliding fit for $\beta, \delta, a, \lambda$ as a function of k, for $l = k$. The results obtained for (5.27) with initial data (5.28) where the plot is for $0 \leq k \leq N$ and $0 \leq l \leq M$ where $N = M = 128$ for the triangles and $N = M = 256$ for the blue curves. The presence of oscillations in the curves at large k are due to aliasing error plus the fact that amplitudes of Fourier coefficients approach machine round off error; therefore, the fits degenerate. Hence, in Figure 5.6, we do not present the fits for all modes due to the presence of the oscillations in the curves. The curves are cut when the oscillations start. Note that the fitted singularity exponent is $\beta = 0.5$, which corresponds to a square root singularity. This is the same singularity type that was obtained for the traveling wave solution, and it is the generic complex singularity for Burger's equation.

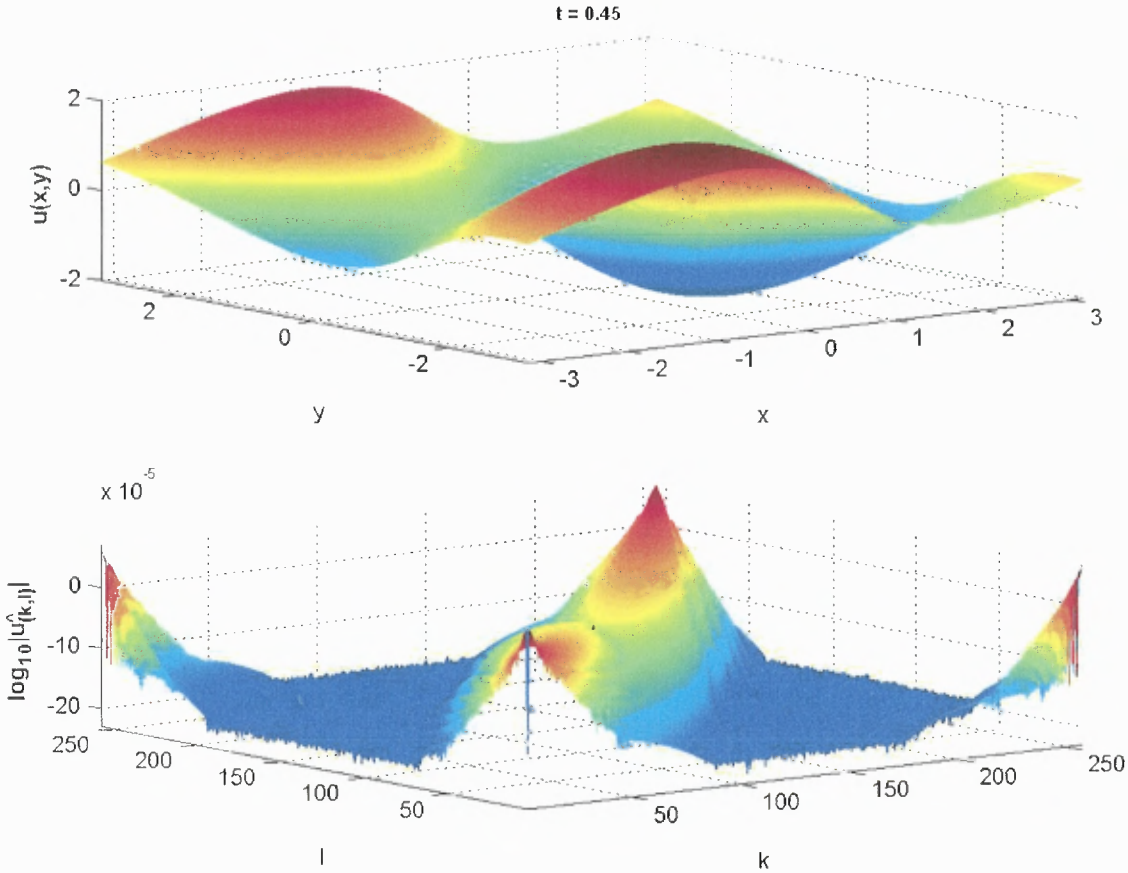

Figure 5.5 The top plot is the numerical solution of equation (5.27) with initial condition (5.28) versus (x, y) at $t = 0.45$. The bottom plot is the Fourier transform of the linear-log scale (i.e., $\log_{10} \left|\hat{u}_{(k,l)}\right|$ versus (k, l)).

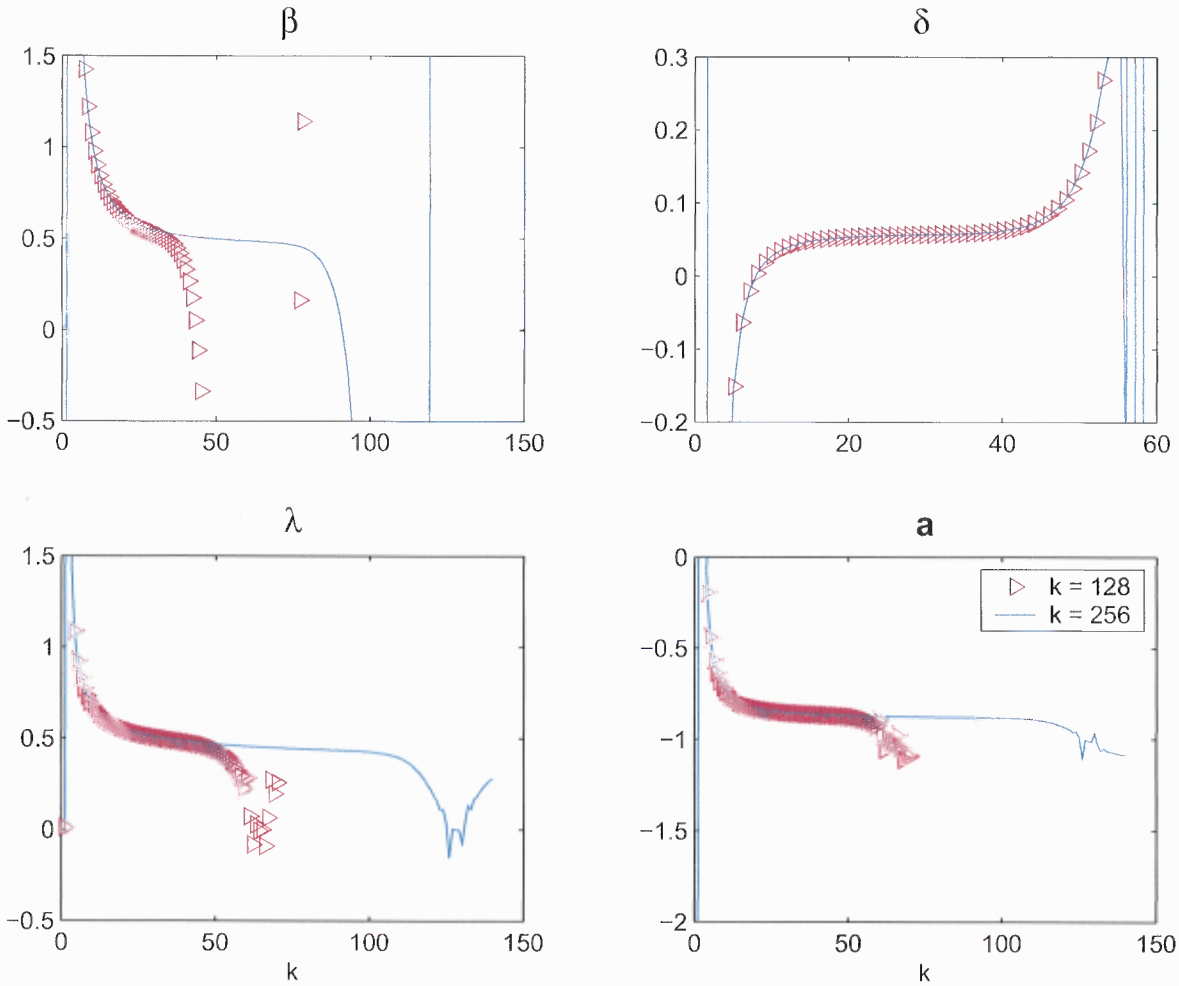

Figure 5.6 Fits for the asymptotic of the β, δ, λ and a for the simplified Burger Equation, i.e., (5.27) with initial condition (5.28). The fits for $k = l = 128$ (triangles) compared to the fits for $k = l = 256$ (blue curves).

For the next example, we consider simplified Burger's equation (5.27) with initial condition of the form (4.7), where we embedded a one over square root singularity, i.e.,

$$u_0 = \mathrm{Re}\left(\frac{1}{\sqrt{1 - \varepsilon_1 \exp(ix) + \varepsilon_2 \sin^2(\frac{y}{2})}}\right) \quad \text{for} \quad \varepsilon_1 = 0.5, \varepsilon_2 = 2. \tag{5.29}$$

Figure 5.7 presents numerical solution of (5.27) with the initial condition (5.29), i.e., u at $t = 1.2$ (the top plot) and its spectrum (the bottom plot). By careful examination of the spectrum of u, i.e., Figure 5.5, one observes that the slowest rate of decay of Fourier coefficients is near the edge, i.e., near $l = 1$. Therefore, in the system of equations (4.23), we fix the direction in wavenumber space in which the matrix is inverted for $l = 1$ and increasing k. The results are similar for other l near 1. The plot is for $0 \leq k \leq N$ and $0 \leq l \leq M$ where $N = M = 256$. Figure 5.8 presents results of the sliding fit for $\beta, \delta, a, \lambda$ as a function of k, for $l = k$. The results obtained for (5.27) with initial data of (5.28) where the plot is for $0 \leq k \leq N$ and $0 \leq l \leq M$ where $N = M = 128$ for the triangles and $N = M = 256$ for the blue curves. The presence of the oscillation in the curves are due to the aliasing error plus the fact that amplitudes of Fourier coefficients approach machine round off error; therefore, the fits degenerate.

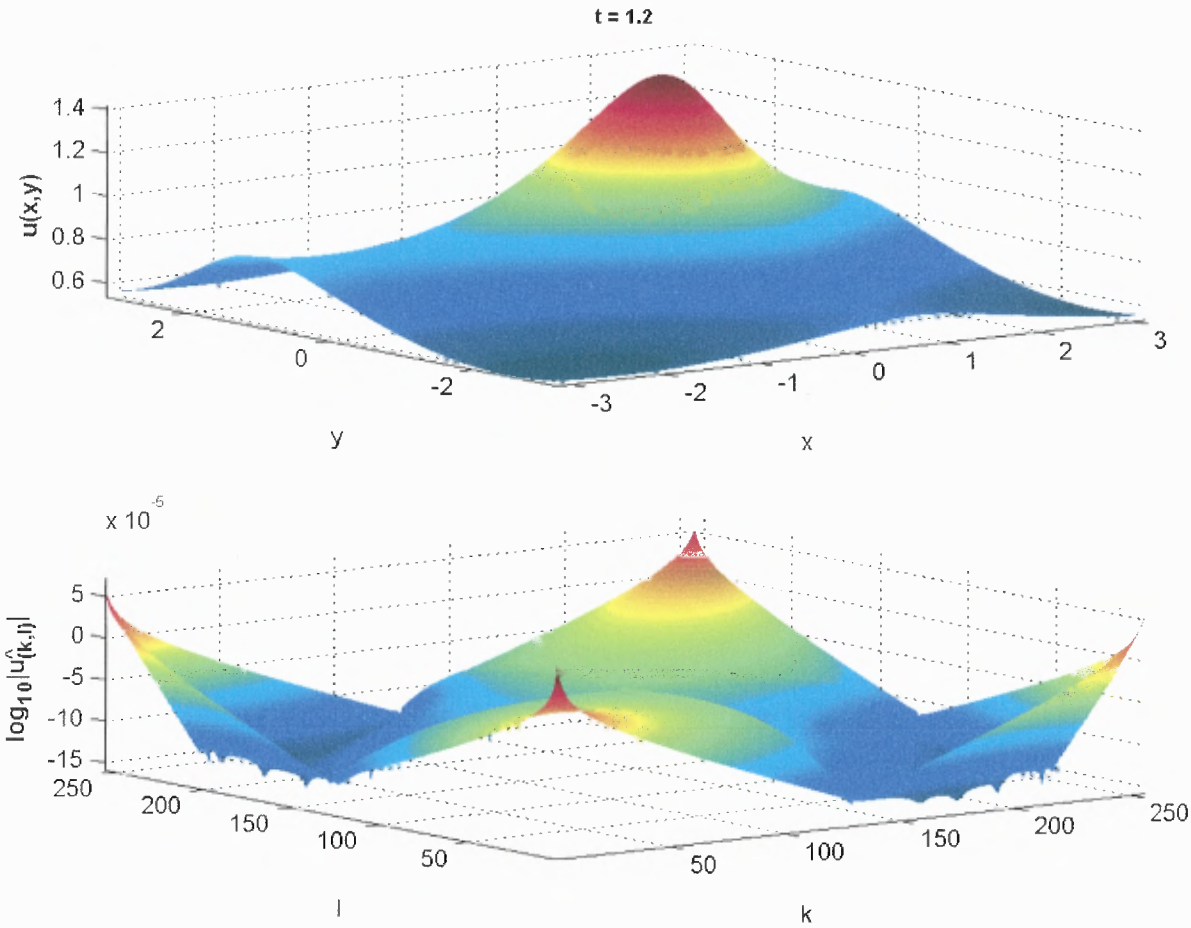

Figure 5.7 The top plot is the numerical solution of (5.27) with initial condition (5.29) versus (x, y) at $t = 1.2$. The bottom plot is the Fourier transform of the linear-log scale (i.e., $\log_{10} \left|\hat{u}_{(k,l)}\right|$ versus (k, l)).

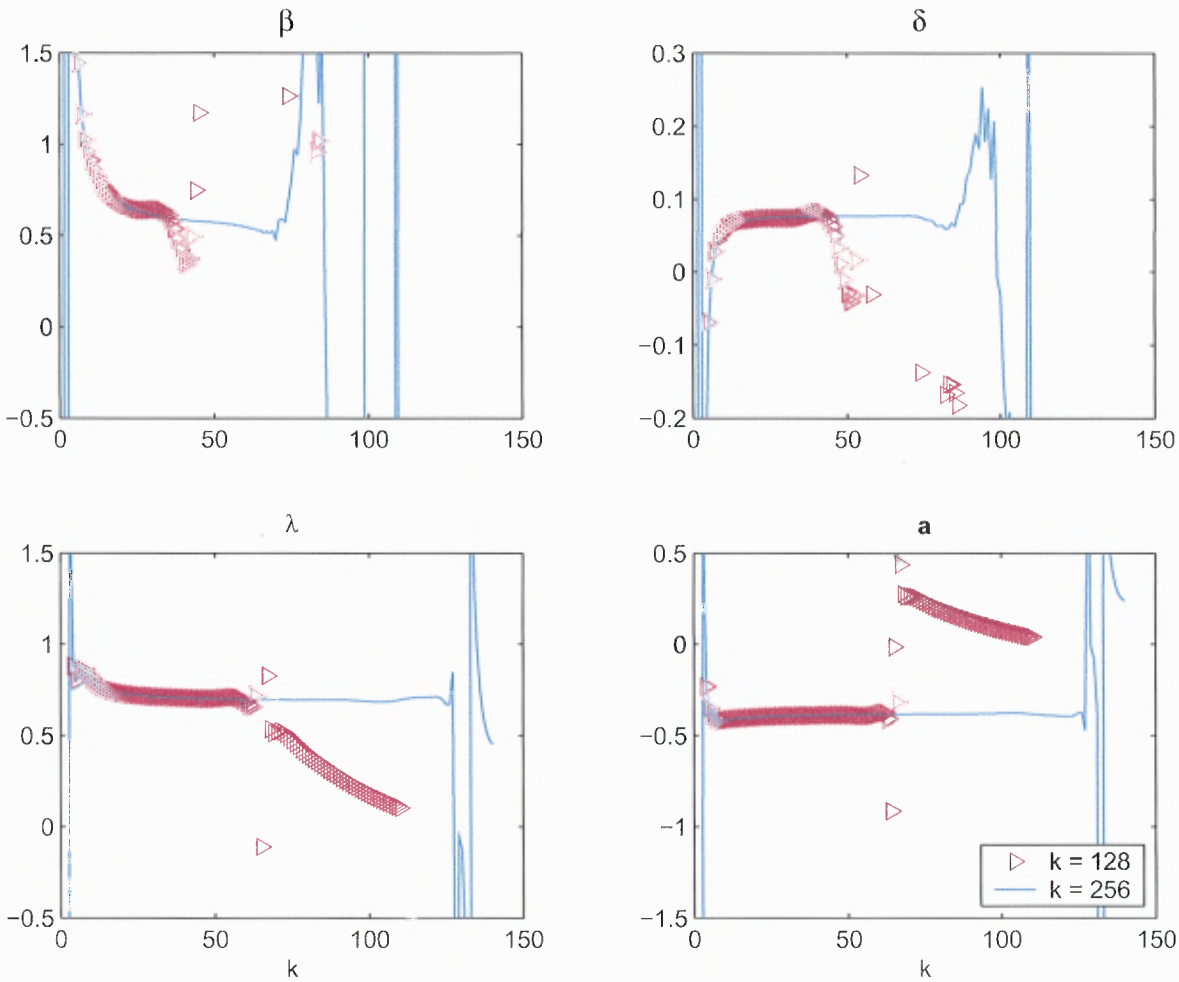

Figure 5.8 Fits for the asymptotic of the β, δ, λ and a for equation (5.27) with initial condition (5.29). The fits for $k = l = 128$ (triangles) compared to the fits for $k = l = 256$ (blue curves).

Note that β approaches the expected values $\frac{1}{2}$ although for the initial condition of the form (5.29) the exponent of the singular curve is $\frac{-1}{2}$. This means that the complex singularities generated by nonlinear term in the equation are closer to the real line than singularities in the initial condition.

5.3 Conclusion

One of the most interesting phenomenon in interfacial fluid dynamics is singularity formation. Examples include pinch off of a liquid thread or self-intersection of a breaking water wave, or the formation of a cusp or curvature singularity on an evolving vortex sheet. Singularity formation can often be understood by analytically extending the variables and equations to the complex plane C, and analyzing the motion of singularities in C. The analytical structure of the solutions in the complex plane can indicate the generic form of singularities. Numerical methods for tracking complex singularities, based on the asymptotic decay of Fourier coefficients, i.e, 1D form fit (2.5) have been successfully applied to Kelvin-Helmholtz instability, [27], [26], [39], and [22] Rayleigh-Taylor instability, [1] and Hele-Shaw flow, [5] among others. However, this method has only been developed for functions of a single variable. In my thesis, I present a new method to analyze the asymptotic behavior of a two or three-dimensional array of Fourier coefficients to detect the location and geometry of singular surface in two and three dimensions. Furthermore, a numerical sliding form fit method is presented. The fitting procedure is validated by computing the (known) singular surface for synthetic data in two and three dimensions. The method also employed for detecting the location and geometry of singular curves for 2D inviscid Burger's equation (5.1) and a simplified version of 2D Burger's equation (5.27).

5.3.1 Future Work

One can employ our numerical method to detect and trace complex singular surfaces for other appropriate multi-dimension partial differential equations. Examples include the equations describing the evolution of a vortex sheet in the 3D Kelvin-Helmholtz or Rayleigh-Taylor flow. Another example is the 2D Boussinessq equations which describes stratified flow under gravity, for which the question of finite time singularity formation is an open problem.

REFERENCES

[1] G. R. Baker, R. Caflisch, and M. Siegel. Singularity formation during Rayleigh-Taylor instability. *J. Fluid Mech.*, 252:51-78, 1993.

[2] G. R. Baker, X. Li, and A. C. Morlet. Analytic structure of two 1D-transport equations with nonlocal fluxes. *Phys. D*, 91:349-375, 1996.

[3] G. R. Baker, D. I. Meiron, and S. A. Orszag. Generalized vortex methods for free-surface flow problems. *J. Fluid Mech.*, 123:477-501, 1982.

[4] G. R. Baker and M. J. Shelley. On the connection between thin vortex layers and vortex sheets. *J. Fluid Mech.*, 215:161-194, 1990.

[5] G. R. Baker, M. Siegel, and S. Tanveer. A well-posed numerical method to track isolated conformal map singularities in Hele-Shaw flow. *J. Comp. Phys.*, 120:348-364, 1995.

[6] J. T. Beale, T. Kato, and A. Majda. Remarks on the breakdown of smooth solution for the 3-D Euler equations. *Comm. Math. Phys.*, 94:61-66, 1984.

[7] D. Bessis and Fournier J. D. Pole condensation and the Riemaan surface associated with a shock in Burger's equation. *J. Physique Lett.*, 45:833-841, 1984.

[8] R Caflisch. Unpublished notes.

[9] R. Caflisch. Singularity formation for complex solution of the 3D incompressible Euler equations. *Physica D*, 67:1-18, 1993.

[10] R. Caflisch, I. Klapper, and G. Steele. Remarks on singularities, dimension and energy dissipation for ideal hydrodynamics and MHD. *Comm. Math. Phys.*, 184:433-455, 1997.

[11] R. Caflisch and M. Siegel. A semi analytic approach to Euler singularities. *Method and Applications of Analysis*, 11(3):423-530, 2004.

[12] G. F. Carrier, M. Krook, and C.E. Pearson. *Function of a Complex Variable.* SIAM, Philadelphia, 2005.

[13] A. J. Chorin and P.J. Bernard. Discretization of vortex sheet with an example of roll-up. *J. of Comp. Phys.*, 13:423-428, 1973.

[14] P. Constantin and A. Fefferman, C. Majda. Geometric constrains on potentially singular solutions for the 3-D Euler equations. *Comm. PDE*, 21:559-571, 1996.

[15] P. G. Drazin and W. H. Reid. *Hydrodynamic Stability.* Cambridge University Press, Cambridge, first edition, 1999.

[16] U. Frisch. *Turbulence, the Legecy of A. N. Kolmogrov.* Cambridge University Press, Cambridge, 1996.

[17] T. Y. Hou, J. S. Lowengrub, and M. J. Shelley. Removing the stiffness from interfacial flows with surface tension. *J. Comp. Phys.*, 114:312-338, 1994.

[18] T. Y. Hou, J. S. Lowengrub, and M. J. Shelley. The long-time motion of vortex sheets with surface tension. *Phys. Fluids.*, 9:1933-1954, 1997.

[19] S. D. Howison. Fingering in Hele-Shaw cells. *J. Fluid Mech.*, 167:439-453, 1986.

[20] S. D. Howison, L. L. Lacey, and J. R. Ockendon. Hele-Show free-boundary problems with suction. *Proc. R. Soc. Edinburg.*, 102:141-152, 1985.

[21] R. Krasny. Desingularization of periodic vortex sheet roll up. *J. of Comp. Phys.*, 65:292-313, 1986.

[22] R. Krasny. A study of singularity formation in a vortex sheet by the point-vortex approximation. *J. Fluid Mech.*, 167:65-93, 1986.

[23] L. D. Landau and E. M. Lifshitz. *Fluid Mechanics.* Pergamon, Oxford, second edition, 1987.

[24] D. Li and Ya. G. Sinai. Blow up of complex solutions of the 3D Navior Stokes system and renormalization group method. *ArXiv:physics/06101v1*, 2006.

[25] A. Majda and A. L. Bertozzi. *Vorticity and Incompressible Flow.* Cambridge University Press, Cambridge, first edition, 2002.

[26] D. I. Meiron, G. R. Baker, and S. A. Orszag. Analytic structure of vortex sheet dynamics. *J. Fluid Mech.*, 114:283-298, 1982.

[27] D. W. Moore. Numerical and analytical aspect of Kelvin-Helmholtz instability. *Theoretical and Applied Mechanics*, 16:263-274, 1984.

[28] D.W. Moore. The spontanous appearance of a singularity in the shape of an evolving vortex sheet. *Proc. R. Soc. Lond.*, 365:105-119, 1979.

[29] D.W. Moore. A vortex method applied to interfacial waves. *In Vortex Motion*, 1982.

[30] D. J. Muraki. A simple illustration of a weak spectral cascade. *SIAM J. Appl. Math.*, 67:1504-1521, 2007.

[31] H. Ockondon and J. R. Ockondon. *Waves and Compressible Flow.* Springer-Verlag, New York, first edition, 2004.

[32] A. G. Orlov. On asymptoics of Taylor coefficients of rational functions of two variables. *Russian Mathematics(Iz. Vuz)*, 37(6):23-30, 1993.

[33] A. G. Orlov. About asymptoics of Taylor coefficients of algebraic functions. *Siberian Math.*, 35:1125-1137, 1994.

[34] M. Paperin. *http://www.brockmann-consult.de/CloudStructures/images/kelvin-helmholtz-instab/k-w-system.gif.* Brockmann Consult, Geesthacht, 2009.

[35] W. Pauls, T. Matsumoto, U. Frisch, and J. Bec. Nature of complex singularities for the 2D Euler equation. *Physics D*, 219(1):40-59, 2006.

[36] G. W. Platzman. An exact integral of complete spectral equations for unsteady one-dimensional flow. *Tellus*, XVI:422-431, 1964.

[37] P. G. Saffman and G. I. Taylor. The penetration of a fluid into a porous medium of Hele-Shaw cell containing a more viscous liquid. *Proc. R. Soc. Lond.*, 245:312-329, 1958.

[38] D. Senouf, R. Caflisch, and N. Ercolani. Pole dynamics and oscillations for the complex Burgers equation in the small-dispersion limit. *Nonlinearity*, 9:1671-1702, 1996.

[39] M. J. Shelley. A study of singularity formation in vortex sheet motion by a spectrally accurate vortex method. *J. Fluid Mech.*, 86(5):2583-2596, 1992.

[40] M. Siegel and R. Caflisch. Calculation of complex singular solutions to the 3D incompressible Euler equations. *Preprint*, 2008.

[41] C. Sulem, P.L. Sulem, and H. Frisch. Tracing complex singularities with spectral methods. *J. of Comp. Phys.*, 50:138-161, 1983.

[42] A. K. Tsikh. Conditions for absolute convergence of series of Taylor coefficients of meromorphic functions of two variables. *Math. USSR Sbornik*, 74:336-360, 1993.

[43] J. A. C. Weideman. Computing the dynamics of complex singularities of nonlinear PDEs. *SIAM J. Applied Dynamical Systems*, 2:171-186, 2003.

[44] X. Yu. *Localized non-blow up conditions for 3D incompressible Euler flows and related equations.* Ph.D thesis, Caltech, 2005.